PLANE SECTIONS OF SYMMETRIC TETRAHEDRAL CONES: INVERSE FIBERS, PONCELET 3-PORISMS, PHASE TRANSITIONS, AND TRIANGLE LOCI

ISMAIL HAMMOUDEH

Abstract. We study the shapes of triangles cut from a one-parameter family of symmetric trihedral cones, equivalently from tetrahedra whose equilateral base is allowed to recede arbitrarily far. A section is described by the cone height h, a downward inclination α, and an azimuth ϕ. The normalized slope $\mu = \tan\alpha/h$ separates elliptic, parabolic, and hyperbolic circumsections at $\mu = 1$. Exact elimination reduces the fixed-height inverse problem to a quartic in μ^2 and exposes the fold, escape, and parabolic boundaries in triangle-shape space. The circumconic–inconic pair is simultaneously projectively equivalent, for every (h, μ), to concentric circles of radii 1 and $1/2$; hence its Poncelet return map is explicit and has exact order three. We determine four collinear distinguished points, prove their barycentric projection formulae, and describe the special right, regular, degenerate, and prism limits. An exact reconciliation with Pinchon's positive-distance classification, combined with a certified analysis of the parabolic divider, gives the complete symmetry-marked refined list of twelve finite transition heights: four change total inverse multiplicity and eight change conic type or event-curve incidence. The regular MPT is certified exactly. For the variable-height parabolic, planar-endpoint, and fixed-transition-star atlases we state explicitly which parts are eliminant root counts, certified examples, or computational observations pending global physical-recovery and connected-cell certificates. Finally, the inverse apex set organizes numerically into strands whose projected axis-intersection locus lies on a quintic. The projected apex and axis-intersection branches join tangentially at a generic scalene acute vertex but have different signed curvatures; the exact curvature jump is computed. Colored Maps of Possible Triangles make the real-algebraic phase structure visible in angle-barycentric and normalized similarity coordinates.

1. Historical setting and scope

The question "which triangles are plane sections of a regular tetrahedron?" has a deceptively elementary statement and a genuinely intricate answer. Folke Eriksson presented the question at the International Congress of Mathematicians in Kyoto in August 1990. He gave two sufficient conditions: two angles larger than $60°$, or all three angle cosines larger than $1/3$. Didier Pinchon recorded this provenance and, in December 1991, completed a much broader computer-algebraic study of plane sections of every regular trihedral angle [6]. His manuscript became Rennes prepublication 92-12 in June 1992. Pinchon classified regions by exact algebraic curves and found fibers with as many as four positive solutions.

Eriksson's later Monthly note [5] again posed the regular tetrahedron case as an unsolved problem. It displayed the angle-barycentric triangle chart and accurately anticipated that the straight sufficient boundaries had to be replaced by curved ones. The note does not cite Pinchon's preprint; the surviving sources do not establish whether Eriksson knew of it. Xia and Yang subsequently used the regular problem as a benchmark for exact isolation of real solutions of semi-algebraic systems [7, Example 7]. Their calculation certified an individual algebraic instance and placed the problem in the computer-vision $P3P$ tradition, but did not supply the geometric atlas developed here.

Date: August 2026.

2020 *Mathematics Subject Classification.* Primary 51M20, 14P10; Secondary 51N20, 68W30.

Key words and phrases. tetrahedral section, regular trihedral angle, Poncelet porism, triangle space, real algebraic geometry, conic section, inverse problem, triangle center.

The present work starts from Pinchon's exact-algebraic viewpoint and extends it in several directions. In particular, the following results appear to be new.

(N1) A uniform h-dependent forward model in which the circumconic type is read from one parameter μ, together with the complete line of four distinguished points C_1, C_2, C_3, C_4 and its projection formulae.

(N2) An explicit simultaneous projectivity from the circumconic–inconic pair to concentric circles of radii 1 and $1/2$, giving a closed formula for the Poncelet return map and proving exact period three throughout the elliptic, parabolic, and hyperbolic affine regimes.

(N3) Fixed-height Maps of Possible Triangles (MPTs), in two coordinate systems, refined simultaneously by inverse multiplicity and conic type; the regular slice is certified, and Pinchon's total counts are transferred exactly to the present half-space convention.

(N4) The exact translation of Pinchon's discriminant and zero-distance loci into the fold and escape boundaries, the reciprocal-distance test for conic type, and the complete symmetry-marked dictionary of twelve finite refined height events.

(N5) Exact eliminants and conjectural/computer-supported classifications for collected parabolic orbits, planar triangle-strand endpoints, and the triangle-star framework originating in *The Triangle Sky*, with certified special cases separated from global claims.

(N6) The numerically traced apex strands, the quintic containment of the C_2 locus, the componentwise complement relations among the projected centers, and the exact curvature jump at every generic scalene acute vertex join.

We use a strict proof-status hierarchy throughout. A *theorem* has a printed proof; a *computer-assisted theorem* additionally has an exact, reproducible certificate; a *certified example* proves one specified instance; a *computational observation* records an exhaustive-looking calculation whose global cell or recovery proof is not yet supplied; and a *conjecture* is not claimed as established. The abstract and conclusion follow the same hierarchy.

The conic picture is also conceptually important. Every section triangle is simultaneously inscribed in the section of the cone's circumcone and tangent to the section of its incone. We prove below that this is an explicit Poncelet 3-porism in the classical projective sense [2], while both conics come from a single spatial construction and four natural distinguished points are collinear. The ellipse–parabola–hyperbola change at $\mu = 1$ is therefore an affine-chart transition, not a change in the projective Poncelet dynamics; the double-line member of the conic pencil makes this isotriviality visible. For modern background on Poncelet dynamics and pencils of quadrics, see [3]; for general projective-conic background see [10]. Neither Eriksson's note nor Pinchon's 53-page preprint uses the terms conic, ellipse, Steiner, or porism in this role. Thus the conic sandwich is not merely a change of language: it organizes the forward map, its limits, and its triangle centers.

2. The symmetric cone and the section parameters

Fix the equilateral base vertices

$$B_k = (\cos(2\pi k/3), \sin(2\pi k/3), 0), \qquad k = 0, 1, 2,$$

and the apex $S = (0, 0, h)$, where $h > 0$. We retain the word *tetrahedron*, while allowing the three lateral edges to continue as forward rays from S through the B_k. The angle β between any two rays satisfies

$$\cos\beta = \frac{h^2 - 1/2}{h^2 + 1}. \tag{1}$$

The base plane section is equilateral. Up to a common similarity and rotation, every other transverse section can be represented by rotating the rays through azimuth ϕ and cutting with

$$\Pi_{h,\mu} : \quad z = -h\mu(x + 1), \qquad \mu = \frac{\tan\alpha}{h}. \tag{2}$$

Here α is the downward angle from the horizontal and the trace of the plane on $z = 0$ is $x = -1$. The apparent singularity at the parabolic position is removed by using μ, or equivalently the downward α.

Proposition 2.1 (Completeness of the plane normalization)**.** *Every finite transverse section of the three forward rays, considered up to similarity, is represented by Equation* (2) *for some* $\mu \geq 0$ *and some azimuth* ϕ.

Proof. Write an arbitrary section plane, after a rotation about the z-axis, as $z = ax + c$. A homothety of positive ratio λ centered at S preserves the triangle shape and changes the plane to

$$z = ax + h + \lambda(c - h).$$

Rotating by π if necessary makes $a \leq 0$. Transversality to the forward rays puts the plane below S, hence $c < h$, and therefore

$$\lambda = \frac{a - h}{c - h} > 0$$

makes the new constant term equal to a. The normalized plane is thus $z = a(x + 1)$. Setting $a = -h\mu$ gives Equation (2). The horizontal case $a = 0$ is included: it is sent to the base plane $z = 0$, corresponding to $\mu = 0$. The discarded rotation is precisely the azimuth ϕ. ☐

Put $\theta_k = \phi + 2\pi k/3$. The kth intersection point is

$$P_k = (t_k \cos\theta_k, t_k \sin\theta_k, h(1 - t_k)), \qquad t_k = \frac{1 + \mu}{1 - \mu\cos\theta_k}. \tag{3}$$

Consequently the plane meets all three forward rays precisely when

$$1 - \mu\cos\theta_k > 0 \qquad (k = 0, 1, 2). \tag{4}$$

In particular every $0 \leq \mu < 1$ is physical for every ϕ. At the parabolic value $\mu = 1$, the three symmetry azimuths $\phi \equiv 0, 2\pi/3, 4\pi/3 \pmod{2\pi}$ are excluded because one denominator vanishes and the corresponding vertex is at infinity. For $1 < \mu < 2$ only restricted azimuths are physical. Thus neither the finite parabolic orbit nor a hyperbolic ϕ-orbit is parametrized by the entire circle.

If a_k^2 is the squared side opposite P_k, then, with indices modulo 3,

$$a_k^2 = (1 + h^2)(t_{k+1}^2 + t_{k+2}^2) + (1 - 2h^2)t_{k+1}t_{k+2}. \tag{5}$$

The three angles follow without approximation from the cosine law,

$$A_k = \arccos\frac{a_{k+1}^2 + a_{k+2}^2 - a_k^2}{2a_{k+1}a_{k+2}}. \tag{6}$$

3. The two conics and the central line

Use orthonormal coordinates (u, v) in the cutting plane, with the u-axis equal to the intersection of that plane with the vertical symmetry plane $y = 0$, and write $d = (1 + h^2\mu^2)^{1/2}$. Direct section of the rotational circumcone and incone gives

$$\mathcal{C}_{\text{out}}: \quad \frac{1 - \mu^2}{d^2}u^2 + v^2 - \frac{2(1 + \mu)}{d}u = 0, \tag{7}$$

$$\mathcal{C}_{\text{in}}: \quad \frac{4 - \mu^2}{d^2}u^2 + 4v^2 - \frac{2(4 + \mu)}{d}u + 3 = 0. \tag{8}$$

The triangle $P_0P_1P_2$ is inscribed in $\mathcal{C}_{\text{out}}$ and its sides are tangent to $\mathcal{C}_{\text{in}}$. The inner conic is always an ellipse on the physical domain $0 \leq \mu < 2$. The outer conic is an ellipse for $\mu < 1$, a parabola for $\mu = 1$, and a hyperbola for $\mu > 1$.

Theorem 3.1 (Line of four distinguished points)**.** *The following signed u-coordinates lie on one central line $L(h)$:*

$$\boxed{C_1 = \frac{1-h^2\mu}{d}, \quad C_2 = d, \quad C_3 = \frac{d}{1-\mu}, \quad C_4 = \frac{d(4+\mu)}{4-\mu^2}.} \tag{9}$$

Here C_1 is the orthogonal projection of the apex onto the cutting plane, C_2 is the intersection with the cone axis, C_3 is the center of the circumconic (finite away from $\mu = 1$), and C_4 is the center of the inellipse.

Proof. The first two coordinates are orthogonal projections in the normal section through the cone axis. Completing the square in Equations (7) and (8) gives the last two. Since all four computations take place on the u-axis, collinearity is intrinsic and independent of ϕ. □

The preceding incidence and tangency statement has the following stronger projective form.

Theorem 3.2 (Explicit Poncelet return map)**.** *For every $h > 0$ and $0 \leq \mu < 2$, the projective closures of $\mathcal{C}_{\text{out}}$ and $\mathcal{C}_{\text{in}}$ are simultaneously projectively equivalent to the concentric circles*

$$\Gamma_0 : X^2 + Y^2 - 2XZ = 0,$$
$$\gamma_0 : 4X^2 + 4Y^2 - 8XZ + 3Z^2 = 0,$$

whose affine radii are 1 and $1/2$. Under the natural angular parametrization of $\mathcal{C}_{\text{out}}$, the two branches of the tangent correspondence are

$$T_{\pm}P_{h,\mu}(\theta) = P_{h,\mu}\left(\theta \pm \frac{2\pi}{3}\right).$$

Consequently $T_{\pm}^3 = \mathrm{id}$, and every real orbit has exact period three. In the rational parameter $z = \tan(\theta/2)$,

$$T_+(z) = \frac{z + \sqrt{3}}{1 - \sqrt{3}z}. \tag{10}$$

The abstract return map is independent of both h and μ.

Proof. In homogeneous cutting-plane coordinates $[U : V : W]$, put

$$\mathcal{P}_{h,\mu}[X : Y : Z] = [dX : (1+\mu)Y : (1+\mu)Z - \mu X]. \tag{11}$$

Its determinant is $d(1+\mu)^2 \neq 0$. Substituting

$$X = \frac{U}{d}, \qquad Y = \frac{V}{1+\mu}, \qquad Z = \frac{W + \mu U/d}{1+\mu}$$

into the equations of Γ_0 and γ_0, and multiplying by $(1+\mu)^2$, gives respectively

$$\frac{1-\mu^2}{d^2}U^2 + V^2 - \frac{2(1+\mu)}{d}UW = 0,$$
$$\frac{4-\mu^2}{d^2}U^2 + 4V^2 - \frac{2(4+\mu)}{d}UW + 3W^2 = 0,$$

the homogeneous forms of Equations (7) and (8).

Parametrize Γ_0 by $P_0(\theta) = [1 + \cos\theta : \sin\theta : 1]$. A chord joining parameters that differ by $2\pi/3$ lies at distance $\cos(\pi/3) = 1/2$ from the common center, and is therefore tangent to γ_0. Thus its two oriented Poncelet steps are $\theta \mapsto \theta \pm 2\pi/3$. Projective maps preserve incidence and tangency, so conjugation by Equation (11) gives the asserted correspondence on the section conics.

It remains to identify this porism with the spatial sections themselves. The intrinsic coordinates used above satisfy $u = d(x+1)$ and $v = y$. Combining this with Equation (3) yields

$$(u(\theta), v(\theta)) = \left(\frac{d(1+\cos\theta)}{1-\mu\cos\theta}, \frac{(1+\mu)\sin\theta}{1-\mu\cos\theta}\right), \tag{12}$$

which is precisely the affine image under $\mathcal{P}_{h,\mu}$ of $P_0(\theta)$. Since the three section vertices have parameters $\phi, \phi + 2\pi/3, \phi + 4\pi/3$, they form one return-map orbit and varying ϕ traverses the porism. Finally, half-angle addition gives Equation (10); its matrix

$$\begin{pmatrix} 1 & \sqrt{3} \\ -\sqrt{3} & 1 \end{pmatrix}$$

has cube $-8I$, hence order three in $\mathrm{PGL}_2(\mathbb{R})$, with no real fixed point. $\square$

Corollary 3.3 (Affine and physical parts of the porism)**.** *For $0 \le \mu < 1$, every real starting point on the circumellipse generates a finite physical section triangle. At $\mu = 1$ the projective return map is unchanged, but the three symmetry azimuths have one vertex at infinity. For $1 < \mu < 2$ the projective hyperbolic porism is still complete, while its finite physical members are exactly the orbits satisfying Equation (4).*

Proof. In Equation (12) the affine chart coordinate is $1 - \mu\cos\theta$. Applying this to the three orbit parameters gives exactly the three inequalities in Equation (4). $\square$

Remark 3.4. After writing $\widehat{u} = u/d$, the two affine equations satisfy

$$F_{\mathrm{in}} = 4F_{\mathrm{out}} + 3(1 + \mu\widehat{u})^2.$$

Thus their pencil contains a double line. This identity is the projective-algebraic fingerprint of the simultaneous circle model. In the prism limit the two conics become the Steiner circumellipse and Steiner inellipse, recovering the affine image of the equilateral configuration.

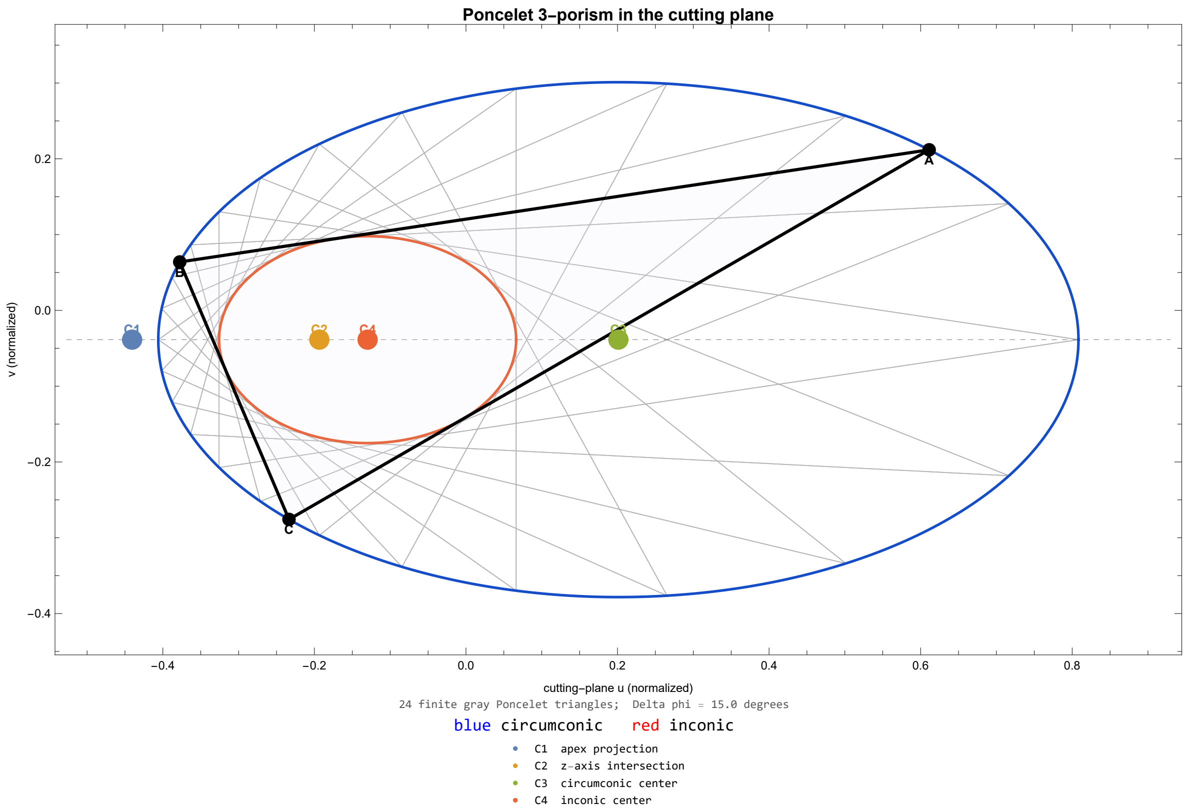

FIGURE 1. Elliptic Poncelet 3-porism at $h = \sqrt{2}$, $\mu = 0.65$, $\phi = 0.40$. The black triangle is the selected member; the light gray triangles sample the orbit every $15°$. Every member is inscribed in the blue circumellipse and tangent to the red inellipse.

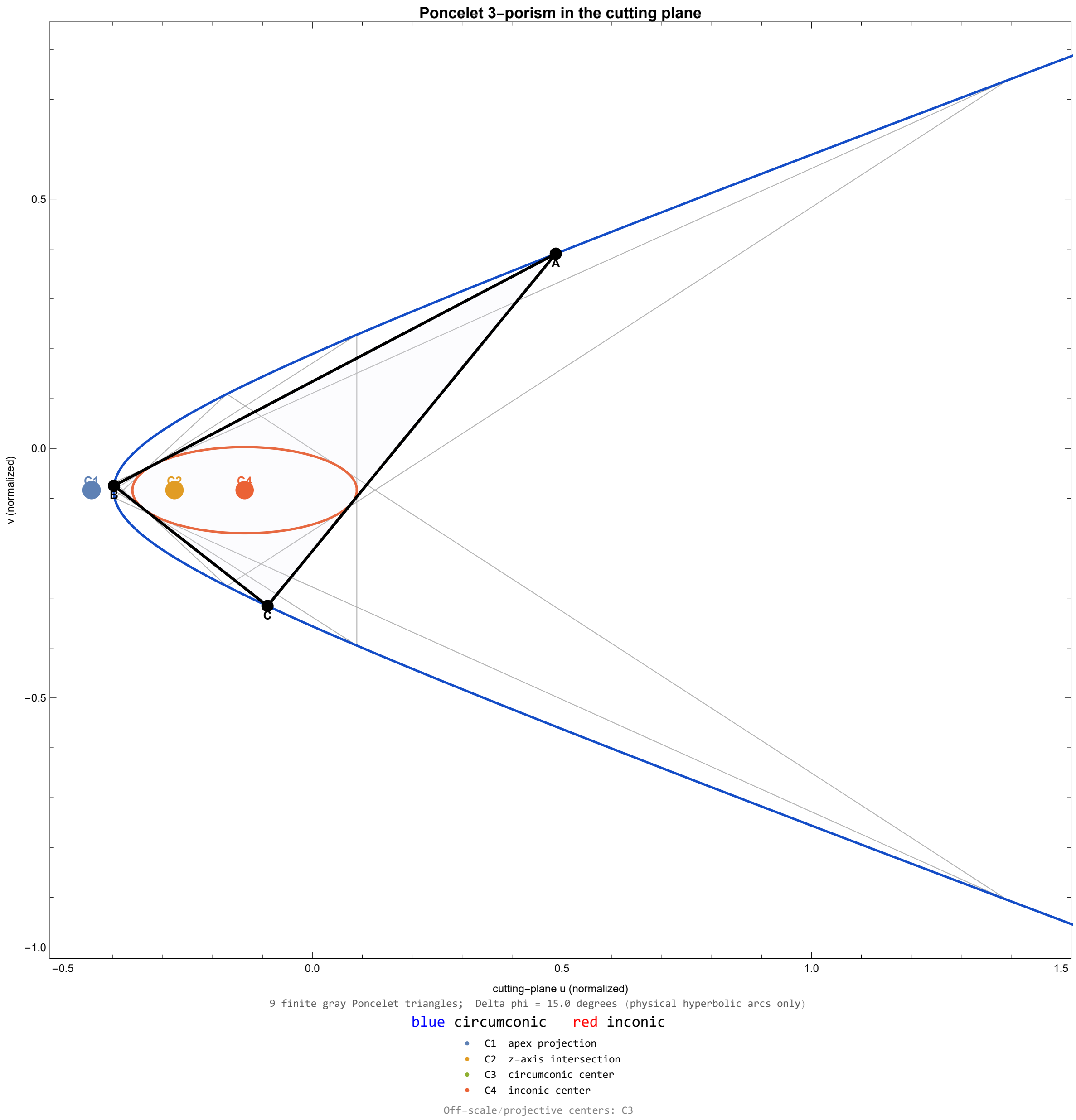

FIGURE 2. Hyperbolic projective Poncelet 3-porism at $h = \sqrt{2}$, $\mu = 1.25$, $\phi = 0.90$. Only physical finite members of the $15°$ sampling are gray; the missing parameter intervals are precisely where a cutting plane fails to meet all three forward rays.

4. TRIANGLE-SHAPE SPACES AND ORBITS

We use two labeled shape charts. In the angle-barycentric chart,

$$(\lambda_1, \lambda_2, \lambda_3) = \frac{1}{\pi}(A_1, A_2, A_3), \qquad \lambda_i > 0, \quad \sum \lambda_i = 1. \tag{13}$$

Thus the whole open equilateral reference triangle represents nondegenerate triangles; its three edges, and only its three edges, represent degenerate triangles. The six chambers cut by $A_i = A_j$ record the six angle orders. Right triangles lie on $A_i = \pi/2$.

In the normalized similarity chart, written in complex notation $C = \xi + i\eta$, normalize

$$A = (-1, 0), \quad B = (1, 0), \quad C = (\xi, \eta), \quad \eta > 0. \tag{14}$$

The squared sides are proportional to

$$((\xi-1)^2+\eta^2,(\xi+1)^2+\eta^2,4).$$

The two charts are related by the sine law, but their algebraic boundaries can look dramatically different. In particular, curves derived for $A=(0,0)$ must not be placed without translation in the normalization Equation (14).

Definition 4.1. At fixed h and α, the *ϕ-orbit* is the image of the physical azimuth interval under the triangle-shape map. At fixed h and ϕ, the *α-orbit* is the image obtained by varying α, or μ, over its physical interval. Their intersection is the produced triangle. A colored chart whose cells record the possible inverse fibers is called a *Map of Possible Triangles*, abbreviated MPT.

5. Invariant reduction and the inverse quartic

Normalize squared sides by $q_i=a_i^2/(a_1^2+a_2^2+a_3^2)$ and put

$$q_1+q_2+q_3=1,\qquad p=q_1q_2+q_2q_3+q_3q_1,\qquad r=q_1q_2q_3. \tag{15}$$

The unordered shape is determined by (p,r) together with the requirement that q_1,q_2,q_3 are positive roots of their cubic. The scalene interior of the unordered quotient is

$$\frac{1}{4}<p<\frac{1}{3},\qquad r>0,\qquad \Delta(p,r)=4p^3-p^2-18pr+27r^2+4r<0, \tag{16}$$

where $\Delta=0$ is the isosceles seam in the unordered quotient.

Because of threefold symmetry, the shape depends on ϕ only through $c=\cos 3\phi$. Let e_j be the elementary symmetric functions of the three t_k in Equation (3). Then

$$\begin{aligned} &D_0=4-3\mu^2-\mu^3c,\\ &e_1=\frac{3(1+\mu)(4-\mu^2)}{D_0},\qquad e_2=\frac{12(1+\mu)^2}{D_0},\qquad e_3=\frac{4(1+\mu)^3}{D_0}. \end{aligned} \tag{17}$$

Put $H=h^2$. Substitution in Equation (5) gives the following explicit rational invariant map. If s_j is the jth elementary symmetric function of the three squared sides, then

$$s_1=2(1+H)e_1^2-3(1+2H)e_2, \tag{18}$$

$$s_2=(1+H)^2e_1^4-3(1+H)(1+2H)e_1^2e_2+3(1+H)(1+3H)e_2^2-9He_1e_3, \tag{19}$$

$$\begin{aligned} s_3={}&(1+H)^3e_1^2e_2^2-(1+H)^2(1+4H)e_2^3\\ &-(1+H)^2(1+4H)e_1^3e_3+9H(1+H)(1+2H)e_1e_2e_3-27H^3e_3^2. \end{aligned} \tag{20}$$

Therefore

$$\boxed{\Psi_h(\mu,c)=\left(\frac{s_2}{s_1^2},\frac{s_3}{s_1^3}\right).} \tag{21}$$

Equations (17) to (21) are a complete printed specification of the forward map; no notebook definition is needed to reconstruct it. Eliminating c produces universal factors $\mu^{24}(\mu-2)^{12}(\mu+2)^{12}$ and one primitive even factor.

Theorem 5.1 (Fixed-height inverse equation)**.** *After removal of the universal factors and primitive normalization, the resultant*

$$\mathrm{Res}_c\big(\mathrm{num}(p-\Psi_{h,1}(\mu,c)),\mathrm{num}(r-\Psi_{h,2}(\mu,c))\big) \tag{22}$$

is a polynomial $F_h(x;p,r)$ of degree at most four in $x=\mu^2$ and is generically quartic. For $x>0$, a root is a physical inverse section if and only if, with $\mu=\sqrt{x}$, there is a $c\in[-1,1]$ satisfying both rational equations $\Psi_h(\mu,c)=(p,r)$ and, for one (equivalently every compatible) solution ϕ of $\cos 3\phi=c$, all three inequalities Equation (4). The root $x=0$ is handled separately and represents only the equilateral section. Thus the quartic supplies candidates, while the two invariant equations and the forward-ray inequalities are the exact necessary-and-sufficient filters. Distinct solutions are taken modulo the threefold rotational symmetry.

Proof. The numerators in Equation (22) are polynomials in c after clearing the common denominator D. Their resultant vanishes for every common solution. Direct factorization gives the three displayed universal factors; the remaining primitive factor is even in μ and has degree eight, hence degree four in $x = \mu^2$. Conversely, the theorem does not infer a section from the resultant alone: it explicitly requires a common recovered c satisfying the original two rational equations and the three strict ray inequalities. Substitution into Equations (3) and (5) then constructs the section. This also explains why roots created by denominator clearing or by projection are rejected. ☐

The five coefficients $[x^0]F_h, \ldots, [x^4]F_h$ are supplied in a machine-readable companion file:

`certificates/GeneralInverseQuartic.wl`

The SHA-256 of its coefficient body is

`3c2a6379d7a75f9e9cf01fdef2fcaeb534addd3c5d811cee43061d71baf79f98`

In particular,

$$[x^4]F_h = H^2\big(48H^3p^2 - 24H^3p + 3H^3 + 48H^2p^2 - 40H^2p + 7H^2 - 20Hp + 72Hr + 5H - 4p + 1\big)^2.$$

Thus exceptional degree drops are explicit and must be retained rather than silently divided away.

Thus four is an upper bound on algebraic candidates at a fixed height; attainment by physical sections follows from Pinchon's exact positive-solution regions, not from the degree alone [6]. The discriminant of F_h detects pair creation and annihilation, but it is not by itself the whole physical boundary: a single branch may also enter or leave through the compactified endpoint $(\mu, c) = (2, -1)$. This distinction between a fold and an escape is essential for the fixed-transition non-nesting phenomenon in Section 10.

For the regular height $h = \sqrt{2}$ there is a particularly economical quartic. Introduce an auxiliary variable u and set

$$v = \frac{1 - 5u + 7u^2 - p(2 - 5u)^2}{2}, \tag{23}$$

$$f(u; p, r) = u^2 - 3u^3 - 3v + 10uv - 8v^2 - r(2 - 5u)^3. \tag{24}$$

An exact root is valid precisely when

$$u > 0, \quad v > 0, \quad u^2 - 4u^3 - 4v - 27v^2 + 18uv \geq 0, \quad 0 \leq 4 - \frac{12v}{u^2} \leq 4. \tag{25}$$

The last quantity is μ^2. The conditions Equations (23) to (25) avoid both numerical approximation and the multi-megabyte logical objects produced by unrestricted symbolic `Solve`; isolating real roots of a single quartic is enough.

The two invariant curves most visible in the regular MPT are

$$\begin{aligned} P(p, r) = {} & 576p^4 - 1248p^3 + 2112p^2r + 724p^2 - 1600pr^2 \\ & - 1072pr - 164p + 416r^2 + 136r + 13 = 0, \end{aligned} \tag{26}$$

$$A_{\text{reg}}(p, r) = 900p^3 - 1737p^2 + 3300pr + 702p - 2500r^2 - 828r - 81 = 0. \tag{27}$$

The first is the parabolic boundary $\mu = 1$; the second is the physical fold caustic. A third physical boundary, easily lost if one studies only the quartic discriminant, is the compactified edge $\mu = 2$:

$$B_{\text{reg}}(p, r) = -1 + 9p - 24p^2 + 16p^3 - 9r + 36pr - 27r^2 = 0. \tag{28}$$

Only the physical subarc is meant in Equation (28); an exact parametrization is

$$p = \frac{27 + 144\ell + 448\ell^2}{(9 + 40\ell)^2}, \qquad r = \frac{3(-3 + 8\ell)^2(1 + 8\ell)}{(9 + 40\ell)^3}, \qquad 0 \leq \ell \leq \frac{3}{8}. \tag{29}$$

Pullback through Equation (13) or Equation (14), not a naive coordinate translation, gives the correct graphical placement of all three curves.

6. Special heights and limiting geometries

The classical Euclidean geometries and the six previously isolated principal heights are summarized in Table 1; the complete twelve-height list appears in Table 5. The opening angle comes from Equation (1).

Table 1. Classical geometries and previously isolated principal heights.

h	β	geometric or bifurcation role
0^+	120^-	planar cone limit; computational FT endpoint prediction
$1/\sqrt{2}$	$90°$	right trihedral angle; fold enters
1	$\arccos(1/4)$	fold-parabolic crossing changes topology
$\sqrt{2}$	$60°$	regular tetrahedron; equilateral escape enters
$\sqrt{H_0}$	$\arccos(a_0/2)$	first Pinchon fold–escape endpoint merger
$\sqrt{3}$	$\arccos(5/8)$	secondary equilateral branch crosses $\mu = 1$
$\sqrt{2+3\sqrt{2}/2}$	$45°$	second Pinchon fold–escape endpoint merger
$+\infty$	0^+	parallel-ray triangular prism limit

6.1. **Right case.** At $h = 1/\sqrt{2}$, the edge rays are pairwise orthogonal. The inverse vertex S is the orthocenter of the spatial right trihedron determined by the section triangle. Exactly the acute triangles occur, each once; right triangles are the boundary and obtuse triangles do not occur. Under orthogonal projection to the section plane, C_1 is the ordinary orthocenter $X(4)$. The other projected centers are naturally defined by the tetrahedral construction but did not match entries in the algebraic search of the current Encyclopedia of Triangle Centers data used in this project. This negative computer search is evidence, not a proof of permanent absence from the ETC.

Indeed, let O be the orthogonal projection of S to the section plane and write $A-S = \rho_A e_A$, and cyclically, where the e_i are pairwise orthogonal unit vectors. Since $S - O$ is normal to the section plane,

$$(A - O) \cdot (C - B) = (A - S) \cdot (C - B) = 0,$$

and the cyclic identities show that O is the orthocenter. Conversely, if O is the orthocenter of a triangle of circumradius R, then the three pairwise scalar products among $A-O, B-O, C-O$ equal $-4R^2 \cos A \cos B \cos C$. Placing S on the normal through O at squared height

$$4R^2 \cos A \cos B \cos C$$

makes $A - S, B - S, C - S$ pairwise orthogonal. This height is positive exactly for an acute triangle, zero for a right triangle, and negative for an obtuse triangle. The positive height is unique in the chosen apex half-space, which proves the asserted existence and multiplicity statement.

6.2. **Regular case.** At $h = \sqrt{2}$ the cone edges meet at $60°$. This is the case studied by Eriksson and Pinchon. We use one fixed apex half-space, so that symmetry does not artificially double the inverse fibers.

Theorem 6.1 (Certified regular MPT)**.** *In a fundamental side-order chamber the complement of the physical event arcs has eight open cells. Their numbers (E, P, H) of elliptic, parabolic, and hyperbolic sections are*

$$(0, 0, 0),\ (0, 0, 1),\ (1, 0, 0),\ (1, 0, 1),\ (2, 0, 0),\ (2, 0, 1),\ (1, 0, 2),\ (3, 0, 0).$$

The same eight labels, repeated by the six permutations of the angles, give the full labeled triangle space. On a regular point of $P(p, r) = 0$, one neighboring elliptic or hyperbolic root is instead parabolic.

Table 2. Exact representatives for all regular open-cell labels. Every interval contains exactly one admissible root u; the appended letter gives its conic type.

(E,P,H)	(ξ,η)	rational isolating intervals for valid u
$(0,0,0)$	$(1/2,1/2)$	none
$(0,0,1)$	$(1/2,1)$	$(2547/10^4, 2548/10^4)_H$
$(1,0,0)$	$(3/4,9/10)$	$(2947/10^4, 2948/10^4)_E$
$(1,0,1)$	$(1/10,3/2)$	$(2951/10^4, 2952/10^4)_H$, $(3305/10^4, 3306/10^4)_E$
$(2,0,0)$	$(1/10,29/20)$	$(3054/10^4, 3055/10^4)_E$, $(3281/10^4, 3282/10^4)_E$
$(2,0,1)$	$(3/10,7/5)$	$(2700/10^4, 2701/10^4)_H$, $(3058/10^4, 3059/10^4)_E$, $(3264/10^4, 3265/10^4)_E$
$(1,0,2)$	$(3/10,3/2)$	$(2807/10^4, 2808/10^4)_H$, $(2863/10^4, 2864/10^4)_H$, $(3299/10^4, 3300/10^4)_E$
$(3,0,0)$	$(1/2,13/10)$	$(2975/10^4, 2976/10^4)_E$, $(3044/10^4, 3045/10^4)_E$, $(3228/10^4, 3229/10^4)_E$

Proof and exact certificate. The topology of the fundamental chamber is Pinchon's exact arc decomposition, refined by the level $\mu = 1$ and by the compactified physical edge. It has the eight components displayed in Figure 3. It remains to show that no physical event curve has been omitted and to label every component.

Write $f = f(u;p,r)$ for Equation (24), after clearing denominators. A simple admissible root varies continuously until either it becomes multiple, reaches one of the equalities in Equation (25), or escapes through a degree drop. Exact elimination gives

$$\begin{aligned}
\mathrm{Res}_u(f, f_u) &= -16(25p-7)^2 A_{\mathrm{reg}}\Delta,\\
\mathrm{Res}_u(f, v) &= 4(25p-7)B_{\mathrm{reg}},\\
\mathrm{Res}_u(f, \tau_{\mathrm{ray}}) &= 16(25p-7)^2\Delta^2,\\
\mathrm{Res}_u(f, \mu^2-1) &= 81P,
\end{aligned}$$

where

$$\tau_{\mathrm{ray}}(u,v) = u^2 - 4u^3 - 4v - 27v^2 + 18uv$$

is the third physical-filter polynomial in Equation (25), and $\Delta = -p^2 + 4p^3 + 4r - 18pr + 27r^2$ is the isosceles discriminant. The remaining endpoint resultants, for $\mu = 0$ and $u = 0$, have no two-dimensional physical image; $25p - 7 = 0$ is the quartic degree-drop factor and likewise supplies no finite admissible root boundary. Thus the only open-cell events are the fold, parabolic, physical escape, degeneracy, and lower-dimensional isosceles mergers already drawn.

For each row of Table 2, exact Sturm counts give one quartic root in every listed rational interval. Quantifier elimination verifies all four filters in Equation (25), verifies the indicated strict inequality $\mu^2 \lesseqgtr 1$, and proves that there is no other admissible root. The executable files `RegularBoundaryCompleteness.wl` and `RegularCellClassification.wl` print `PASS` under Wolfram Language 15.0. Hence the label is constant on, and certified for, every open component. $\square$

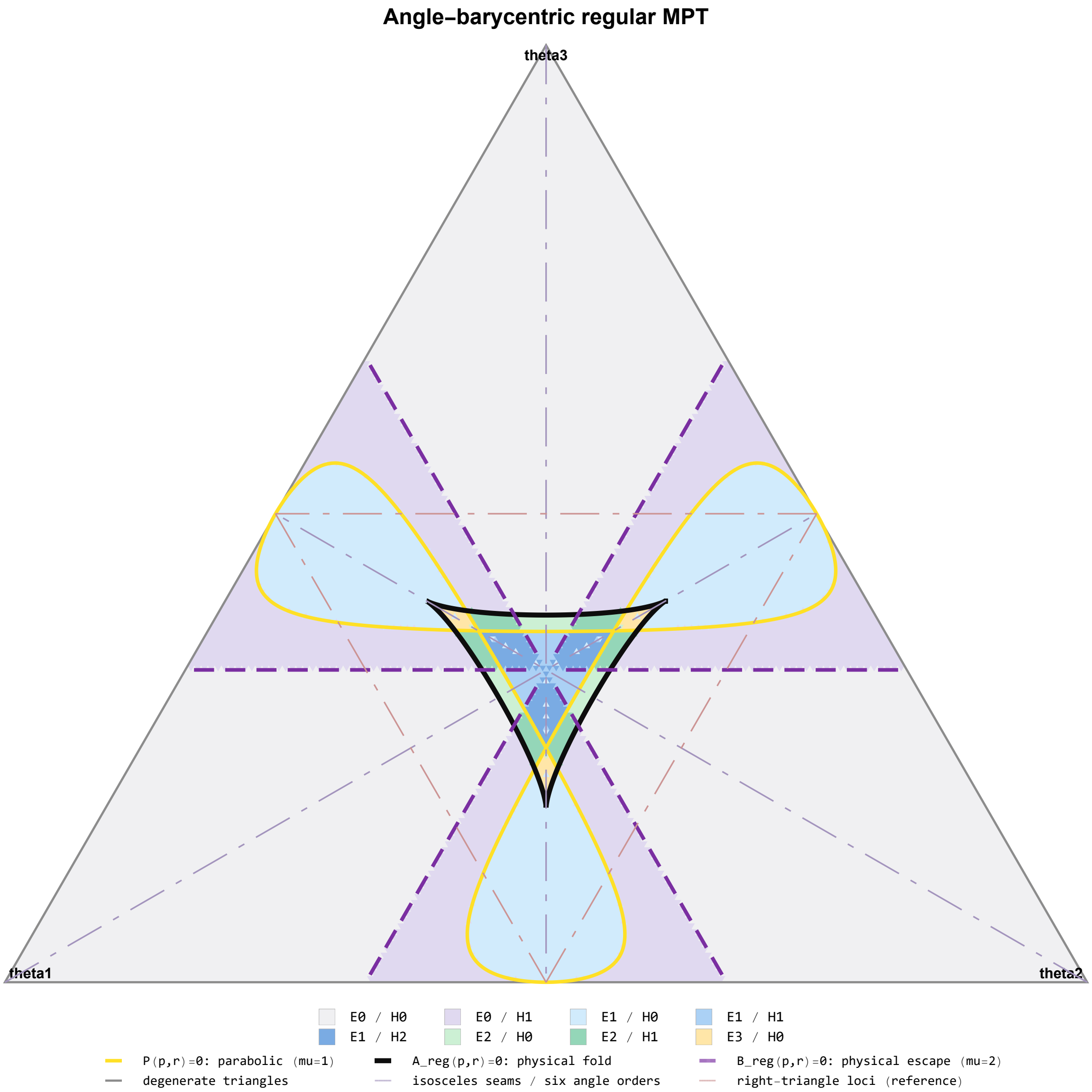

FIGURE 3. The regular angle-barycentric MPT, exported directly by Mathematica as vector graphics. Colors record the full pair E/H. Gold is $P = 0$, black is the physical fold $A_{\text{reg}} = 0$, and purple is the compactified escape arc $B_{\text{reg}} = 0$. Thin dash-dotted curves show isosceles and right-triangle reference loci; only the boundary of the reference triangle represents degenerate triangles.

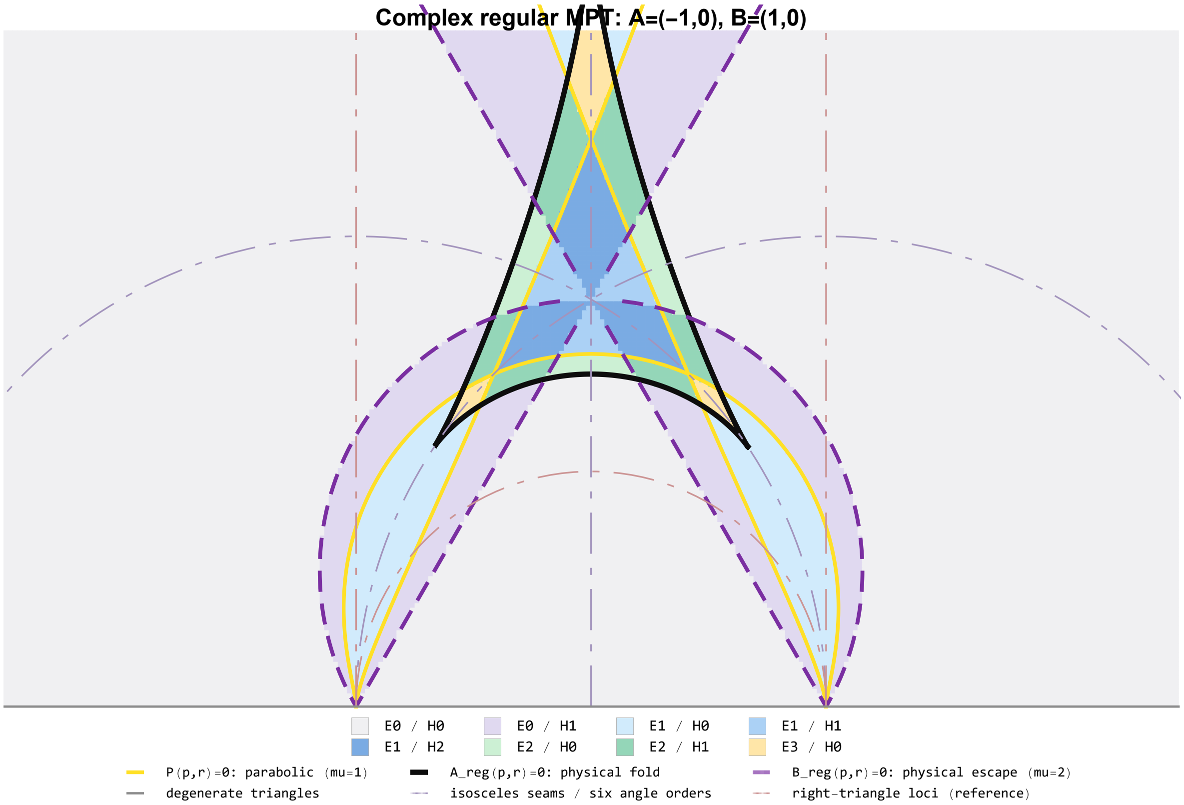

FIGURE 4. The same certified regular cells in the complex chart $A = (-1, 0)$, $B = (1, 0)$, $C = (\xi, \eta)$. The common legend and colors are identical to Figure 3; the exact pullback prevents the displaced or disconnected spurious curves produced by using an $A = (0, 0)$ formula.

Pinchon supplied the global regular-region classification and multiplicities; Eriksson publicized the problem and the sharp shape question, while Xia–Yang later used one resulting semialgebraic system as an algorithmic test case. Relative to those works, Theorem 6.1 adds the explicit elliptic/parabolic/hyperbolic refinement, the compactified physical-edge boundary, exact machine-checkable representatives, and matched MPTs in the two coordinate charts. The two conics and the line $C_1C_2C_3C_4$ add further geometric structure not used in the earlier classifications.

6.3. **Prism case.**

Proposition 6.2 (Unique prism realization)**.** *In the parallel-ray limit, every nondegenerate labeled triangle has exactly one realization, up to similarity and the fixed apex half-space convention. That realization is elliptic. Its two section conics are the Steiner circumellipse and Steiner inellipse.*

Proof. Write a plane transverse to the parallel rays as a graph with slope vector $g \in \mathbb{R}^2$. Its induced planar metric is
$$M = I + gg^{\mathsf{T}}.$$
Conversely, the labeled affine map from an equilateral reference triangle to the prescribed triangle determines its positive-definite metric up to a common scalar. Normalize its smaller eigenvalue to one. The resulting matrix has eigenvalues 1 and $\lambda \geq 1$, hence $M - I$ is positive semidefinite of rank at most one and equals gg^{T}. Thus g is recovered up to sign. The two signs give congruent sections related by the reflection convention inherited from the finite-apex problem; fixing that convention selects one. Transversality makes the circumsection an ellipse. Affine equivalence with the equilateral section then identifies the two conics as the Steiner pair; see [4]. □

Consequently, as $h \to \infty$,
$$C_2 = C_3 = C_4 = G = X(2),$$
while C_1 recedes to the point at infinity on the principal axis. In the ETC convention this is the corresponding infinite center (identified in our search with $X(3413)$). Phase 13 is the last *finite*-height phase $H_A < H < \infty$; the prism $H = \infty$ is a separate limiting stratum. This case explains why the finite-height MPT tends to one all-elliptic cell from the center outward.

6.4. **Degenerate case.**

As $h \to 0^+$, the cone becomes planar. Numerical continuation predicts that one physical inverse-apex branch tends to the Fermat–Torricelli point when all angles are below 120°, merges with the corresponding vertex at 120°, and disappears beyond 120°. This remains part of the computational planar-endpoint observation in Section 9, not a theorem used elsewhere in the rigorous core.

7. Pinchon reconciliation and height bifurcations

7.1. **Dictionary with Pinchon's opening parameter.**

Pinchon writes $a_{\mathrm{P}} = 2\cos\beta$ for the common trihedral opening. From Equation (1),
$$a_{\mathrm{P}} = \frac{2H-1}{H+1}, \qquad H = \frac{a_{\mathrm{P}}+1}{2-a_{\mathrm{P}}}, \qquad H = h^2. \tag{30}$$
Let a_0 be the root in $(1, \sqrt{2})$ of $a_0^3 + 2a_0^2 - 4 = 0$, and let $H_0 = (a_0+1)/(2-a_0)$. Equivalently,
$$4H_0^3 - 8H_0^2 - 4H_0 - 1 = 0, \qquad H_0 \simeq 2.4498438945, \quad h_0 \simeq 1.5651977174.$$

Table 3. Common parameter dictionary after exact reconciliation. Pinchon's a_0 and $\sqrt{2}$ are genuine total-multiplicity transitions; $H = 1$ and $H = 3$ are additional transitions of the elliptic/parabolic/hyperbolic refinement.

H	h	a_{P}	β	mechanism and present proof status
$1/2$	$1/\sqrt{2}$	0	$90°$	proved fold–boundary collision; right trihedron
1	1	$1/2$	$\arccos(1/4)$	proved fold–parabolic collision
2	$\sqrt{2}$	1	$60°$	regular tetrahedron; proved compactified entry
H_0	$\sqrt{H_0}$	a_0	$\arccos(a_0/2)$	fold endpoint meets the compactified escape boundary; total count changes
3	$\sqrt{3}$	$5/4$	$\arccos(5/8)$	proved secondary equilateral branch crossing $\mu = 1$
$2+3\sqrt{2}/2$	$\sqrt{2+3\sqrt{2}/2}$	$\sqrt{2}$	$45°$	second fold–escape merger; total count changes

Proposition 7.1 (Exact Pinchon–present correspondence)**.** *Let $x, y, z > 0$ be Pinchon's distances from an inverse apex to the three vertices, and put $\sigma_1 = 1/x$, $\sigma_2 = 1/y$, $\sigma_3 = 1/z$. Positive solutions of Pinchon's system (11) are in bijection with physical forward-ray sections in the present normalization, modulo similarity and reflection in the section plane. Their normalized plane slope is determined by*

$$\mu^2 = \frac{4(Q-P)}{S^2}, \qquad S = \sigma_1 + \sigma_2 + \sigma_3, \quad Q = \sum_i \sigma_i^2, \quad P = \sum_{i<j} \sigma_i\sigma_j. \tag{31}$$

Consequently $0 \le \mu < 2$ and

$$\mu^2 - 1 = \frac{3(Q-2P)}{S^2}. \tag{32}$$

Thus $Q < 2P$, $Q = 2P$, and $Q > 2P$ give respectively the elliptic, parabolic, and hyperbolic members of Pinchon's positive fiber.

Under this bijection Pinchon's curve Γ_b is the non-isosceles fold image $K = 0$, while his loci D_x, D_y, C_{1z}, C_{2z} on which one of x, y, z vanishes are precisely the three chart branches of the compactified escape boundary $\mu = 2$. His boundary counts and open-cell multiplicities therefore equal the total $E + P + H$ counts in our MPTs.

Proof. Choose unit ray vectors e_i with $e_i \cdot e_j = a_{\mathrm{P}}/2$. Our unnormalized ray vectors have squared length $1+H$ and mutual scalar product $H - 1/2$. Hence, on writing the ray parameters as t_i and $x_i = \sqrt{1+H}\, t_i$, their squared endpoint distances satisfy

$$(1+H)(t_i^2 + t_j^2) + (1-2H)t_it_j = x_i^2 + x_j^2 - a_{\mathrm{P}} x_i x_j,$$

which is exactly Pinchon's system after the common similarity normalization. Conversely, three positive distances along the fixed rays give a plane through their endpoints and hence a physical section.

The three reciprocal distances are samples of an affine linear form on three directions separated by $2\pi/3$. After division by their mean they have the unique form

$$\frac{3\sigma_i}{S} = 1 - \mu\cos(\phi + 2\pi i/3).$$

Taking the squared norm of the zero-sum part gives Equation (31). Moreover $4 - \mu^2 = 12P/S^2 > 0$, and subtraction of one gives Equation (32). If one of x, y, z tends to zero, the corresponding reciprocal dominates and $\mu^2 \to 4$, proving the escape identification. For the fold statement, put

$$J = \det \frac{\partial(p, r)}{\partial(\mu, c)}, \qquad \Delta_q = -p^2 + 4p^3 + 4r - 18pr + 27r^2,$$

and define the second, distinct denominator polynomial

$$E = 8 - 2\mu^2 + 4H\mu^2 + 2c\mu^3 + 4cH\mu^3 + \mu^4 + H\mu^4.$$

Direct substitution into the invariant map gives the exact identity

$$243(c^2-1)E^6J^2 = 16\mu^2 D_0^4 K(\mu,c;H)^2\Delta_q. \tag{33}$$

In the open physical scalene domain, $\mu D_0 E(c^2-1)\Delta_q \neq 0$; therefore $J=0$ if and only if $K=0$. Pinchon's Γ_b is precisely his remaining non-isosceles positive-solution collision discriminant. The positive-solution bijection already proved therefore carries Γ_b exactly to the physical fold image, rather than merely to a curve with the same qualitative interpretation. □

All identities in the proof, including Equation (33), are checked in exact arithmetic by `PinchonReconciliation.wl`; its decisive output is `PINCHON RECONCILIATION: PASS`.

TABLE 4. Theorem-by-theorem precedence and translation. A dash means that the cited source does not treat that result; *imported* means that this paper uses Pinchon's theorem rather than claiming a new proof.

statement	prior work and exact location	status here
positive distance system and physical realization	Pinchon, equations (11) and following paragraph; Xia–Yang, regular semialgebraic system in Example 7; Eriksson, challenge formulation only	identical system under Equation (30); bijection explicit
isosceles multiplicities	Pinchon, Theorem 1; Eriksson, right-isosceles obstruction	imported; thresholds translated to H
general existence criterion	Pinchon, Theorem 2; Eriksson, two sufficient regular conditions	imported, including the non-elementary γ_2^+ alternative
general positive-fiber counts	Pinchon, Sections 3.2–3.3; Xia–Yang, one exact regular instance	imported total counts; displayed in matched charts
remaining discriminant curve Γ_b	Pinchon, equations (17)–(20); Eriksson anticipated a curved regular boundary	identified with the physical fold image $K=0$
zero-distance loci	Pinchon, equations (21), (23), (25), (27)	identified with compactified escape $\mu=2$
conic type of each solution	not separated by Pinchon, Eriksson, or Xia–Yang	new reciprocal-distance test Equation (32)
centers and enveloping conics	not treated by the three predecessors	present geometric refinement

The physical inverse fold is governed in (μ, c) coordinates by

$$K(\mu,c;H) = 4-(1+2H+4H^2)\mu^2 - H(1+2H)\mu^3 c, \qquad H=h^2. \tag{34}$$

The exact comparison with Pinchon settles total multiplicity. The remaining refined transitions are found by following the parabolic divider through the fold, compactified escape, and isosceles strata.

Definition 7.2 (Symmetry-marked refined MPT type)**.** Let $\overline{\mathcal{T}}$ be the compact angle-barycentric triangle-shape domain. A *symmetry-marked refined MPT* is its finite semialgebraic stratification by the degenerate boundary, the parabolic, physical-fold, and compactified-escape sets, and the three isosceles/permutation seams, with each open cell labeled by its inverse count $(\mathrm{E},\mathrm{P},\mathrm{H})$ of elliptic, parabolic, and hyperbolic realizations. Two such MPTs have the same labeled combinatorial type if a semialgebraic homeomorphism of $\overline{\mathcal{T}}$ preserves each named stratum, every seam label, and every $(\mathrm{E},\mathrm{P},\mathrm{H})$ cell label. If the seam labels are forgotten one obtains the coarser intrinsic inverse-fiber MPT. The twelve-level theorem below concerns the symmetry-marked refinement; in particular the seam incidences at $\mathcal{H}_7$ and $\mathcal{H}_{10}$ are genuine marked transitions even when the coarser cell adjacency is unchanged.

Define H_G, H_E, H_T, H_B by

$$\begin{aligned}
0 &= 64H_G^6 + 336H_G^5 + 608H_G^4 + 328H_G^3 - 300H_G^2 - 259H_G - 48,\\
0 &= 16H_E^3 - 24H_E^2 - 51H_E + 16,\\
0 &= 65536H_T^8 - 106496H_T^7 - 219392H_T^6 - 98080H_T^5 + 14237H_T^4\\
&\qquad + 25931H_T^3 + 8815H_T^2 + 1249H_T + 64,\\
0 &= 4H_B^4 - 12H_B^3 - 8H_B^2 + 1,
\end{aligned}$$

where H_G is the unique positive root and H_E, H_T, H_B are the indicated larger positive roots. Exact rational isolating intervals are

$$\frac{7425}{10^4} < H_G < \frac{7426}{10^4}, \quad \frac{2583}{10^3} < H_E < \frac{2584}{10^3}, \quad \frac{2928}{10^3} < H_T < \frac{2929}{10^3}, \quad \frac{3556}{10^3} < H_B < \frac{3557}{10^3}.$$

Put $H_A = (11 + \sqrt{129})/4$.

We denote the twelve critical squared-height levels by $\mathcal{H}_1, \dots, \mathcal{H}_{12}$ in increasing order. For a fixed triangle, the actual stars on level $\mathcal{H}_i$ are $T_i^{(1)}, \dots, T_i^{(N_i)}$; thus N_i is a fiber count, not the name of a height. The stars $T_1^{(j)}$ are exactly the orthostars at $H = 1/2$. Graphical labels T_i suppress the branch superscript. Explicitly,

$$\begin{array}{llll}
\mathcal{H}_1 = \frac{1}{2}, & \mathcal{H}_2 = \frac{5}{7}, & \mathcal{H}_3 = H_G, & \mathcal{H}_4 = 1,\\
\mathcal{H}_5 = 2, & \mathcal{H}_6 = H_0, & \mathcal{H}_7 = H_E, & \mathcal{H}_8 = H_T,\\
\mathcal{H}_9 = 3, & \mathcal{H}_{10} = H_B, & \mathcal{H}_{11} = 2 + \frac{3\sqrt{2}}{2}, & \mathcal{H}_{12} = H_A.
\end{array} \tag{35}$$

Lemma 7.3 (Parabolic arc)**.** *The parabolic image $P_H(c) = \Psi_H(1, c)$, $-1 \le c \le 1$, is the embedded rational arc*

$$\begin{aligned}
p_P &= \frac{48H^2c^2 + 120H^2c + 75H^2 + 52Hc^2 + 220Hc + 214H + 16c^2 + 76c + 151}{12(4Hc + 5H + 2c + 7)^2},\\
r_P &= -\frac{(c-1)^2(4H^3c^2 - 4H^3 - 36H^2c - 45H^2 - 60Hc - 102H - 16c - 65)}{54(4Hc + 5H + 2c + 7)^3}.
\end{aligned}$$

Its only changing incidences with the isosceles seams occur at $H = 1/2$ and $H = 3$.

Proof. One has

$$\frac{dp_P}{dc} = \frac{6(H+1)^2(c-1)}{(4Hc + 5H + 2c + 7)^3} < 0 \quad (-1 \le c < 1),$$

and

$$\Delta(P_H(c)) = \frac{(c-1)^3(c+1)L_H(c)^2}{108(4Hc + 5H + 2c + 7)^6}.$$

Here $\operatorname{Disc}_c L_H = 432H^3(H+1)^3$, $L_H(1) = 27(H+1)^2(2H-1)$, and $L_H(-1) = -(H-3)^2(2H+3)$. □

Lemma 7.4 (Physical fold)**.** *Put $x = \mu^2$ and*

$$c_F = \frac{4 - (1 + 2H + 4H^2)x}{H(1+2H)x^{3/2}}.$$

The fold image is the rational parametrization

$$\begin{aligned}
p_F &= \frac{16 + 32H + 64H^2 - 8Hx - 64H^2x - 32H^3x + (3H^2 + 12H^3 + 12H^4)x^2}{12(1+2H)^2(-2+Hx)^2},\\
r_F &= \frac{(1+H)(-1+2H)^2(1+4H)[-16 - 8Hx + (H + 4H^2 + 4H^3)x^2]}{54(1+2H)^4(-2+Hx)^3}.
\end{aligned}$$

It is a physical embedded arc on

$$\frac{4}{(1+2H)^2} \le x \le \frac{1}{H^2}$$

only for $H > 1/2$. At $H = 1/2$ it coincides with the physical boundary, and for $0 < H < 1/2$ it has no interior physical part.

Proof. The relevant physical boundary is $c_\partial = (4 - 3\mu^2)/\mu^3$, and direct subtraction gives

$$c_F - c_\partial = \frac{(H+1)(2H-1)(\mu-2)(\mu+2)}{H(2H+1)\mu^3}. \tag{36}$$

For $0 \le \mu \le 1$, every azimuth is physical. On the hyperbolic part $1 < \mu < 2$, (36) has the physical-boundary sign precisely when $H > 1/2$; equality holds at $H = 1/2$. The endpoint values of c_F are 1 and -1. Moreover,

$$\frac{dp_F}{dx} = -\frac{H(2H-1)^2(Hx+4)}{3(2H+1)^2(Hx-2)^3} > 0,$$

because $Hx < 2$ in the interior of the physical interval. Thus p_F is strictly monotone and the physical fold image is embedded. Substitution into the parabolic eliminant gives $(x-1)^2 R_H(x)$, where

$$\begin{aligned} R_H(x) = {}& H^2(1+2H)^4x^4 + 8H(-1-5H-6H^2+4H^3+8H^4)x^3 \\ &+ 8H(-1+7H+8H^2+12H^3)x^2 + 32(-1+2H-3H^2+2H^3)x \\ &+ 16(5-10H+H^2). \end{aligned}$$

Moreover

$$\begin{aligned} \mathrm{Disc}_x\, R_H ={}& -2^{24}H^3(H+1)^3(2H-1)^4(2H+1)^4(4H+1)^4(27H^2+19H+4), \\ R_H\left(\frac{4}{(1+2H)^2}\right) ={}& \frac{16(H+1)(2H-1)^2(2H+3)(2H^2-11H-1)}{(2H+1)^4}, \\ R_H(1/H^2) ={}& \frac{(4H^4-12H^3-8H^2+1)^2}{H^6}. \end{aligned}$$

Thus the physical fold–parabolic events are $H = 1, H_B, H_A$. A later fold–escape resultant also contains the algebraic factor $4H^2 + 5H - 3$. Its positive root $H = (\sqrt{73} - 5)/8 < 1/2$ is rejected by (36); it is algebraic, but not a physical transition. $\square$

Lemma 7.5 (Escape arc)**.** *The blow-up $\mu = 2-\varepsilon$, $c = -1+\ell\varepsilon^2$ gives the embedded compactified escape arc $0 \le \ell \le 3/8$,*

$$\begin{aligned} p_E &= \frac{(H+1)(192H\ell^2 + 48H\ell + 3H + 64\ell^2 + 48\ell + 21)}{3(16H\ell + 2H + 8\ell + 5)^2}, \\ r_E &= \frac{(H+1)^2(8\ell-3)^2(32H\ell + 8\ell + 9)}{27(16H\ell + 2H + 8\ell + 5)^3}. \end{aligned}$$

Its only changing parabolic incidences occur at $H = 5/7$ and $H = H_E$.

Proof. Direct differentiation gives

$$\frac{dp_E}{d\ell} = \frac{32(H+1)(4H+1)(8\ell-3)}{3(16H\ell + 2H + 8\ell + 5)^3} < 0 \qquad (0 \le \ell < 3/8),$$

so p_E is strictly monotone and the escape image is embedded. Substitution into the parabolic eliminant gives a quartic $S_H(\ell)$. In increasing powers of ℓ, its coefficients are

$$[\ell^0] : 3840 - 29856H + 61767H^2 + 5907H^3 - 78000H^4 + 10656H^5 + 19968H^6 - 5376H^7,$$

$$[\ell^1] : 28672 - 30464H - 129696H^2 + 106976H^3 - 90112H^4 - 61440H^5 + 163840H^6 + 237568H^7,$$

$$[\ell^2] : -16384 - 161792H + 24192H^2 + 997504H^3 + 346112H^4 - 258048H^5 - 65536H^6 - 1409024H^7,$$

$$[\ell^3] : 49152H + 399360H^2 + 571392H^3 - 2162688H^4 - 5111808H^5 + 4718592H^7,$$

$$[\ell^4] : -36864H^2 - 380928H^3 - 983040H^4 + 1179648H^5 + 6291456H^6 + 3145728H^7.$$

Its discriminant is

$$\operatorname{Disc}_\ell S_H = -580284393415022003858964448\, H^3(H+1)^8(2H-1)^{18}(4H+1)^4 \cdot (4H^3+11H^2+5H+1)^2(52H^3+156H^2+93H+16),$$

and its endpoint values are

$$S_H(0) = -3(7H-5)(16H^3-24H^2-51H+16)^2,$$
$$S_H(3/8) = 12288(H+1)^3(2H-1)^4.$$

The stated events follow by Sturm isolation. □

Lemma 7.6 (Triple incidences)**.** *The only physical triple incidences among the parabolic, fold, and escape strata occur at $H = H_G$ and $H = H_T$.*

Proof. Eliminating between the fold and escape parametrizations gives the displayed sextic for the same-preimage point $x = 1$ and the displayed degree-eight polynomial for the other parabolic branch. Exact Sturm isolation leaves one physical root of each, namely H_G and H_T; all quotient factors and the smaller roots are nonphysical. □

Lemma 7.7 (Stratified semialgebraic triviality)**.** *Let $\mathcal{E} \subset (0,\infty)\times\overline{\mathcal{T}}$ be the union of the named event strata in Definition 7.2, with their finite intersection stratification, and let $\pi(H,q) = H$. On the complement of the twelve levels in (35), π has no critical value on any stratum. Consequently the symmetry-marked refined MPT type is constant over each intervening open interval.*

Proof. The arc and incidence lemmas, together with Pinchon's four total-multiplicity events, exhaust projection-critical points, boundary passages, and multiple intersections. The exact factor and Sturm checks are recorded in `certificates/RefinedTransitionCompleteness.wl`.

Let I be one of the thirteen open height intervals and let $J \Subset I$ be compact. Choose a finite semialgebraic Whitney stratification of $J \times \overline{\mathcal{T}}$ compatible with all named event sets, seams, their intersections, and the inverse-count cells. The exact critical-value calculation shows that π restricts to a submersion on every stratum over J. Since $\overline{\mathcal{T}}$ and J are compact, the projection is proper. The semialgebraic version of Thom's first isotopy lemma therefore gives a stratum-preserving semialgebraic trivialization over J, compatible with every named set and cell [12, 11]. Hence it preserves all marks and labels in Definition 7.2. Any two heights in I lie in such a compact J, so the marked MPT type is constant throughout I. □

Theorem 7.8 (Complete symmetry-marked twelve-height phase theorem)**.** *Apart from $H = 0$ and the separate prism stratum $H = \infty$, the symmetry-marked refined inverse-fiber MPT changes type exactly at the twelve levels in (35), and nowhere else. The four levels $\mathcal{H}_1, \mathcal{H}_5, \mathcal{H}_6, \mathcal{H}_{11}$ change total physical multiplicity. The other eight change conic type or marked event incidence. At $H = \infty$, Proposition 6.2 gives one elliptic realization for every nondegenerate triangle.*

TABLE 5. Before/at/after witnesses that every listed level is an actual transition of the symmetry-marked refined event network.

level	h approximately	just below	at the level	just above
$\mathcal{H}_1$	.707107	no physical fold arc	boundary fold; orthostar	interior fold arc; total count changed
$\mathcal{H}_2$	.845154	two $P \cap E$ points	one reaches the escape endpoint	one interior $P \cap E$ point
$\mathcal{H}_3$	.861720	one $P/F/E$ incidence order	triple point	reversed incidence order
$\mathcal{H}_4$	1	$x = 1$ fold–parabolic contact is physical	contact at the fold endpoint	$x = 1$ lies outside the fold interval
$\mathcal{H}_5$	1.414214	no secondary equilateral branch	secondary branch at $\mu = 2$	one additional physical equilateral branch
$\mathcal{H}_6$	1.565198	first fold/escape endpoint order	coincident endpoints	reversed order; total count changed
$\mathcal{H}_7$	1.607434	$P \cap E$ on one side of seam	$P \cap E$ on isosceles seam	$P \cap E$ on the other side
$\mathcal{H}_8$	1.711179	one interior $P/F/E$ order	triple point	reversed order
$\mathcal{H}_9$	1.732051	secondary equilateral branch hyperbolic	secondary branch parabolic ($\mu = 1$)	secondary equilateral branch elliptic
$\mathcal{H}_{10}$	1.885936	$P \cap F$ on one side of seam	$P \cap F$ on isosceles seam	$P \cap F$ on the other side
$\mathcal{H}_{11}$	2.030104	second fold/escape endpoint order	coincident endpoints	reversed order; total count changed
$\mathcal{H}_{12}$	2.364203	one finite $P \cap F$ point	endpoint contact	no finite $P \cap F$ point

Proof. Pinchon's Theorems 1 and 2 and the sign-cell discussion in his Section 3.3 show that total positive-fiber patterns change exactly at $a_{\mathrm{P}} = 0, 1, a_0, \sqrt{2}$. The parameter dictionary (30) sends these values to $\mathcal{H}_1, \mathcal{H}_5, \mathcal{H}_6, \mathcal{H}_{11}$. The remaining rows follow from Lemmas 7.3 to 7.6; their exact endpoint factors and local root counts give the before/at/after invariants in Table 5. Thus every listed value is attained as an actual transition. The exhaustion and constancy assertions are Lemma 7.7. All factorizations, physical intervals, Sturm counts, resultants, isolating intervals, and ordering assertions are checked in exact arithmetic by `certificates/RefinedTransitionCompleteness.wl`, whose decisive output is `REFINED TWELVE-HEIGHT CERTIFICATE: PASS`. □

The atlas below gives one sample in each of the thirteen open finite-height phases; adjacent panels therefore bracket every value in Table 5.

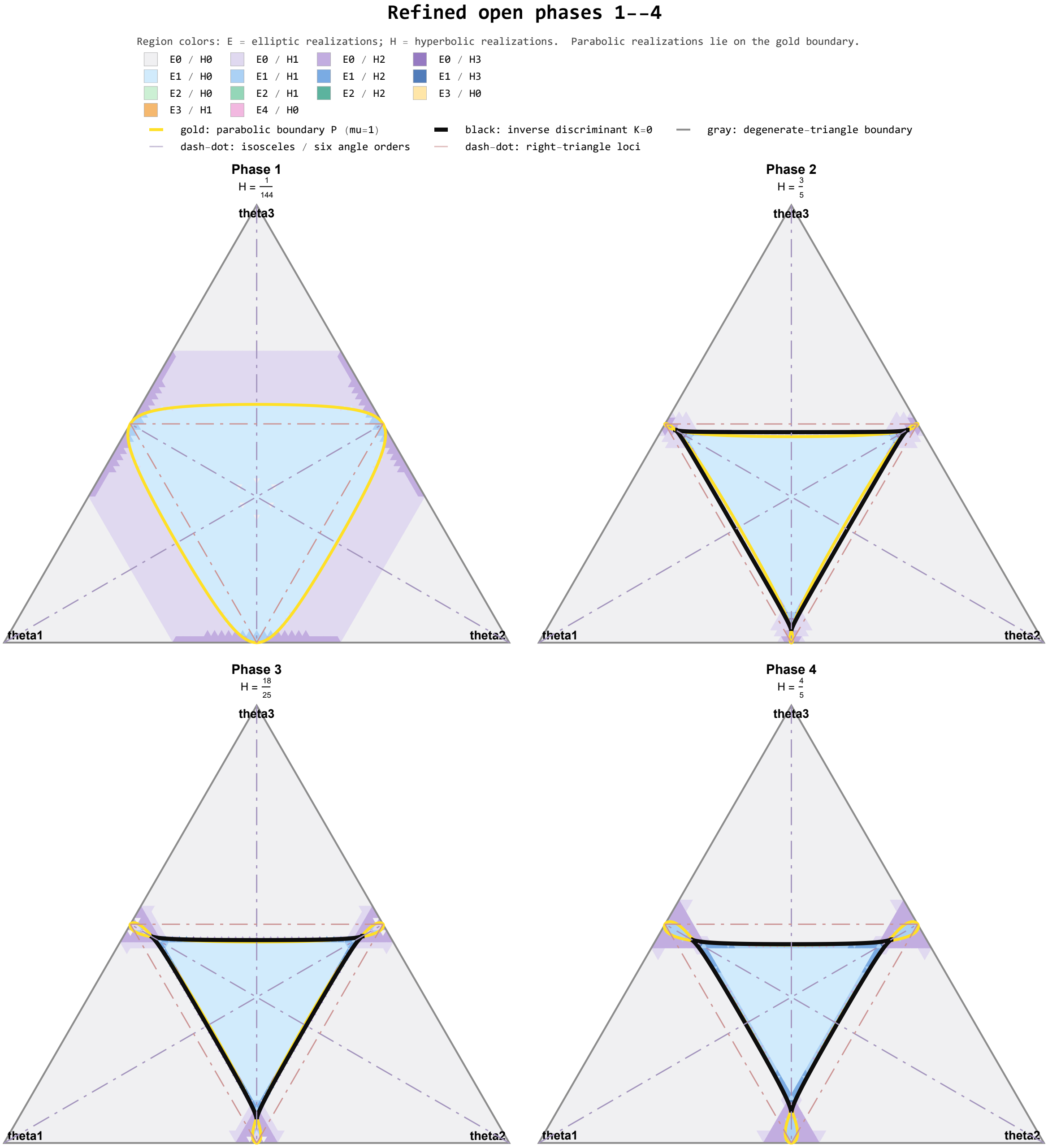

FIGURE 5. Refined phase atlas, part I: samples in the first four open intervals, separated by $H = 1/2, 5/7, H_G$. Colors record computed (E, H) counts; gold is $\mu = 1$, black is the physical fold, and gray is the degenerate locus. This first panel set supplies the common legend for Figures 5 to 8.

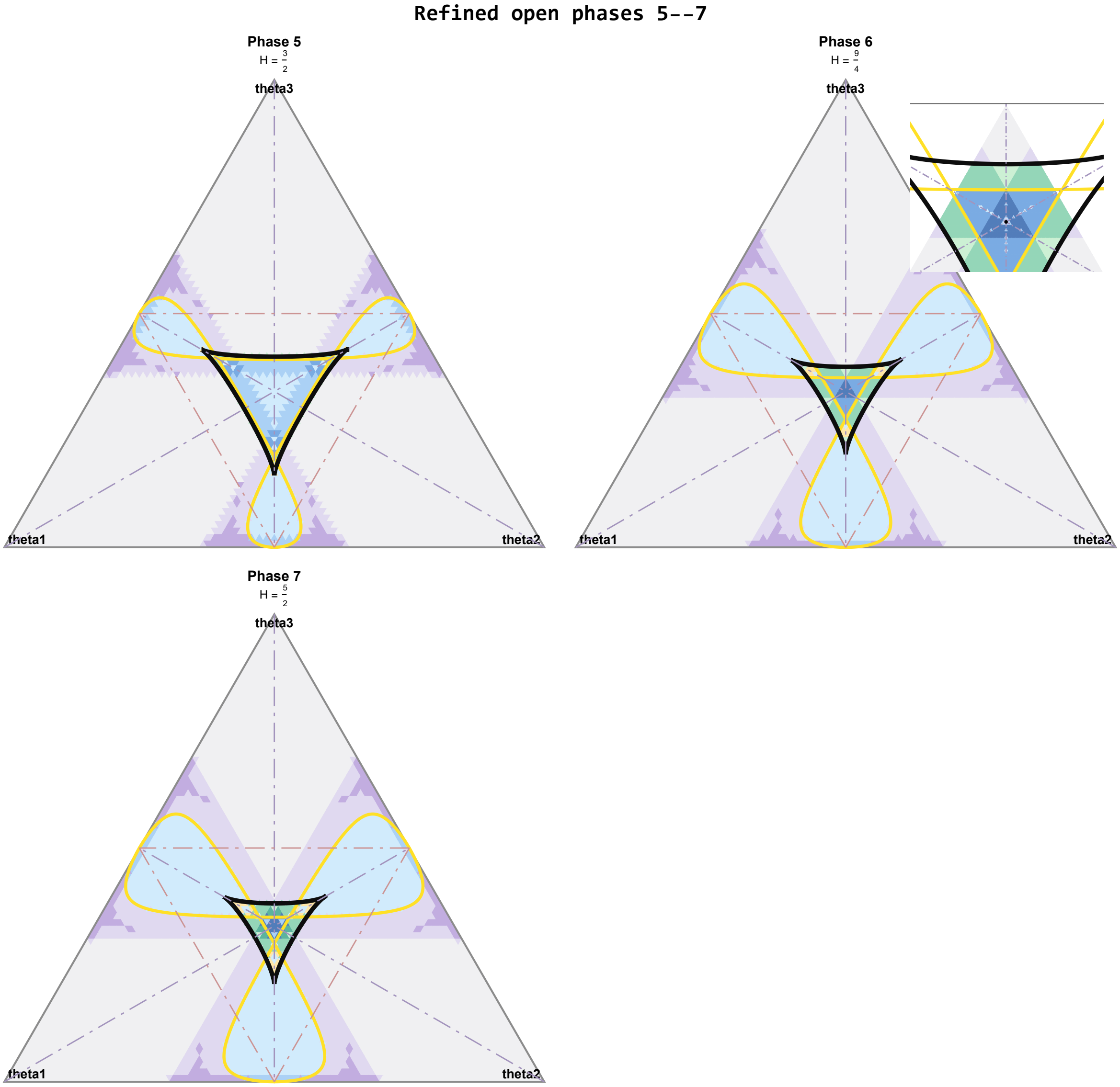

FIGURE 6. Refined phase atlas, part II: samples in phases 5–7, separated by $H = 2, H_0, H_E$; the preceding boundary $H = 1$ lies between parts I and II. The common legend is in Figure 5.

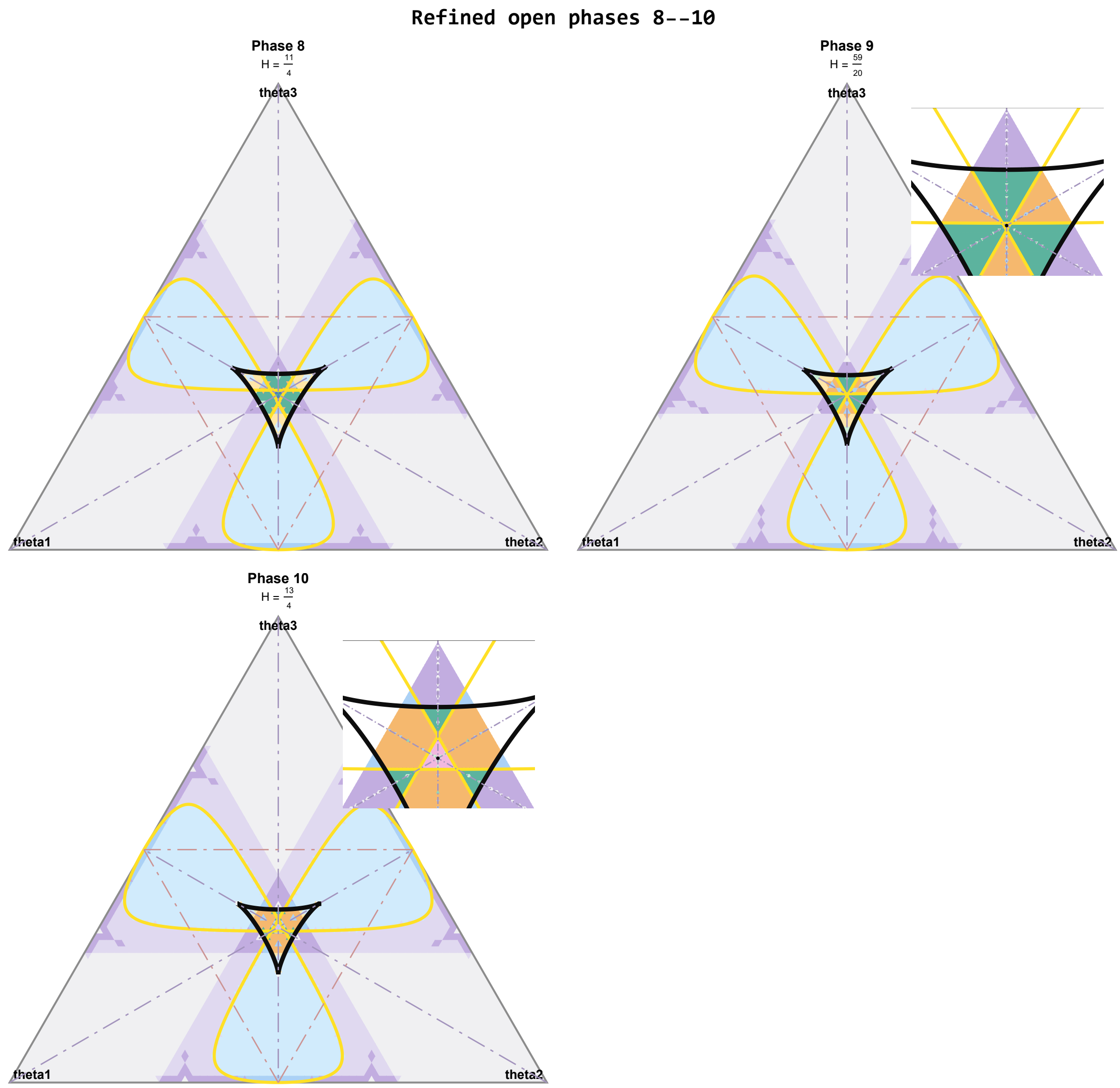

FIGURE 7. Refined phase atlas, part III: samples in phases 8–10, separated by $H = H_T, 3, H_B$. Insets resolve the equilateral neighborhoods; the common legend is in Figure 5.

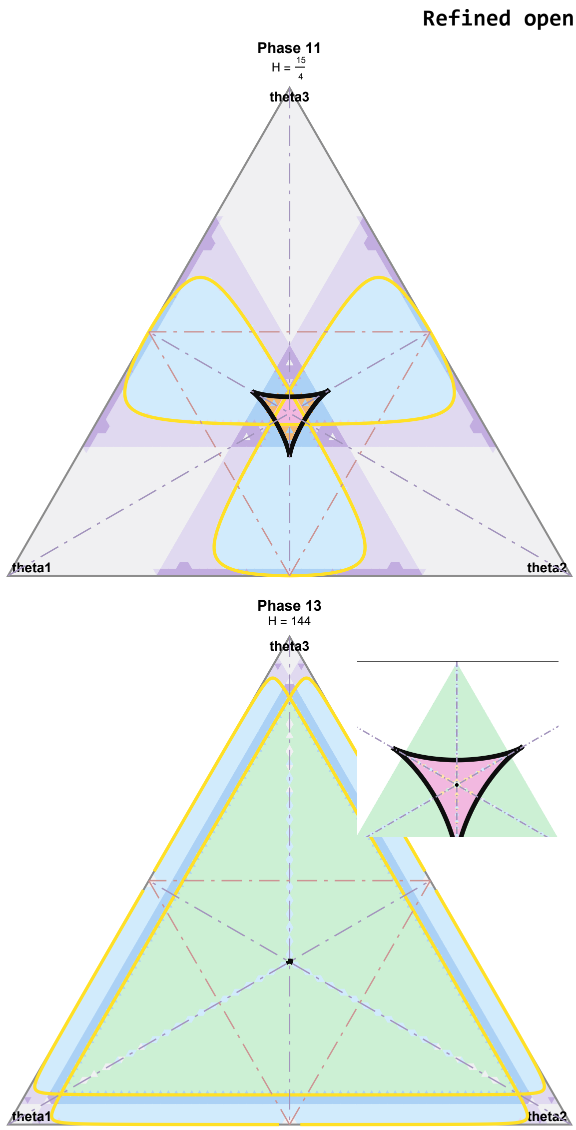

FIGURE 8. Refined phase atlas, part IV: samples in phases 11–13, separated by $H = 2 + 3\sqrt{2}/2$ and H_A, followed by a near-prism sample. Together, Figures 5 to 8 bracket all twelve finite transition heights of Theorem 7.8; the common legend is in Figure 5.

For bookkeeping relative to the twelve values in Table 5, we use the right-continuous convention: every critical slice is owned by the neighboring larger-H phase. Counts on the slice itself are nevertheless evaluated exactly: a multiple fold root is counted once, a root at $\mu = 1$ is parabolic, and $\mu = 2$ is excluded as a compactified zero-distance limit. Phase ownership therefore never changes a boundary multiplicity. It only removes ambiguity in captions and tables.

The next three sections form a computational extension of the rigorous fixed-height core. They retain exact eliminants, exact special examples, and clearly stated local results, but their colored global atlases are not used in the proofs above. Each missing connected-cell or physical-recovery step is stated once at the result it affects.

8. The variable-height parabolic eliminant

Set $\mu = 1$ and eliminate c from $\Psi_h(1, c) = (p, r)$. With $H = h^2$ the primitive equation is a quintic

$$Q(H; p, r) = 0, \qquad [H^5]Q = 3(4p-1)^4, \qquad [H^0]Q = 16(3p-1)G_0(p, r), \tag{37}$$

where

$$\boxed{G_0 = -7 + 57p - 120p^2 + 16p^3 - 108r + 432pr - 432r^2.} \tag{38}$$

The full quintic is unambiguously and compactly defined as the primitive degree-five factor of

$$\mathrm{Res}_c\big(\mathrm{num}(p - \Psi_{\sqrt{H},1}(1, c)), \mathrm{num}(r - \Psi_{\sqrt{H},2}(1, c))\big)$$

normalized by Equation (37). The complete expanded quintic and the quantified real-algebraic tests used below are supplied in `certificates/ParabolicHeightMultiplicity.wl`.

Proposition 8.1 (Certified positive-root count for the parabolic eliminant)**.** *On the scalene nondegenerate domain, the number of distinct positive roots of $Q(H; p, r)$ is locally constant on every connected component of $G_0 \neq 0$. The exact samples $(q_1, q_2, q_3) = (1/5, 3/10, 1/2)$ and $(1/7, 2/7, 4/7)$ certify respectively a three-root component with $G_0 > 0$ and a two-root component with $G_0 < 0$. At a regular crossing of $G_0 = 0$, one root reaches $H = 0$ and is excluded.*

On the isosceles stratum $(q_1, q_2, q_3) = (a, a, 1 - 2a)$, $1/6 < a < 1/2$, the number is 2 for $a \le 7/30$ and 3 for $a > 7/30$, except

$$a = \frac{3 + \sqrt{33}}{36} \quad \textit{has 2}, \qquad a = \frac{1}{3} \quad \textit{has 1.}$$

Proof. The isosceles factorization is

$$\begin{aligned} Q = {}& (2a-1)^3\big(-7 + 30a + 3(2a-1)H\big) \\ & \times \big(4 - 24a + 36a^2 + (5 - 36a + 36a^2)H + (1 - 12a + 36a^2)H^2\big)^2. \end{aligned}$$

For scalene triangles, the discriminant factors as

$$\mathrm{Disc}_H\, Q = -557256278016(4p-1)^{12}\Delta^2 A B^2, \tag{39}$$

where

$$\begin{aligned} A = {}& -125 + 1200p + 4512p^2 - 61696p^3 + 129792p^4 - 19008r \\ & + 179712pr - 414720p^2r - 635904r^2 + 2654208pr^2, \\ B = {}& p + 4p^2 - 80p^3 + 192p^4 + 3r + 180pr - 1328p^2r + 2240p^3r \\ & + 460r^2 - 288pr^2 - 5184p^2r^2 + 3456r^3. \end{aligned}$$

For reproducibility, the two quantified statements actually eliminated are

$$\neg\exists(q_1, q_2, q_3, p, r)\,[\,\mathcal{T}(q, p, r) \wedge A(p, r) = 0\,], \qquad \neg\exists(q_1, q_2, q_3, p, r)\,[\,\mathcal{T}(q, p, r) \wedge B(p, r) = 0\,],$$

where $\mathcal{T}$ consists of

$$q_i > 0, \quad \sum q_i = 1, \quad 4p - 1 > 0, \quad \prod_{i<j}(q_i - q_j) \neq 0, \quad p = \sum_{i<j} q_i q_j, \quad r = q_1 q_2 q_3.$$

Wolfram Language `Resolve[...,Reals]` returns `False` for both existential formulas. Hence only $H = 0$, namely $G_0 = 0$, changes the open-cell count. Exact sample certificates are

(q_1, q_2, q_3)	(p, r)	$\operatorname{sign} G_0$	$\#\{H > 0 : Q(H; p, r) = 0\}$
$(1/5, 3/10, 1/2)$	$(31/100, 3/100)$	$+$	3
$(1/7, 2/7, 4/7)$	$(2/7, 8/343)$	$-$	2.

The last column is obtained by exact Sturm counting. The companion file, written for Wolfram Language 15.0, contains these four executable tests and has SHA-256

`6ab9139b83c62010a7b1c40fdc57c2d45643bfe1787a3e5dad7e447c5d6ca091`

□

Computational observation 8.2 (Physical parabolic recovery)**.** For every tested open cell, each positive root counted in Proposition 8.1 recovers a common $c \in [-1, 1]$ satisfying the original two invariant equations and all forward-ray inequalities. The global claim that these are exactly the physical parabolic heights remains pending two certificates: connectedness (or direct quantified root counts) for every relevant sign region of the scalene (p, r) domain, and quantified physical recovery for every positive root of Q. Consequently the colored plot below is presently an eliminant-root MPT supported by physical sampling, not yet a global physical-section theorem.

In the complex chart Equation (14), the boundary $G_0 = 0$ becomes

$$\begin{aligned} 0 = \; & -27 + 54\eta^2 - 27\eta^4 + 4\eta^6 + 108\xi^2 - 162\eta^2\xi^2 + 54\eta^4\xi^2 \\ & - 162\xi^4 + 162\eta^2\xi^4 - 27\eta^4\xi^4 + 108\xi^6 - 54\eta^2\xi^6 - 27\xi^8. \end{aligned} \tag{40}$$

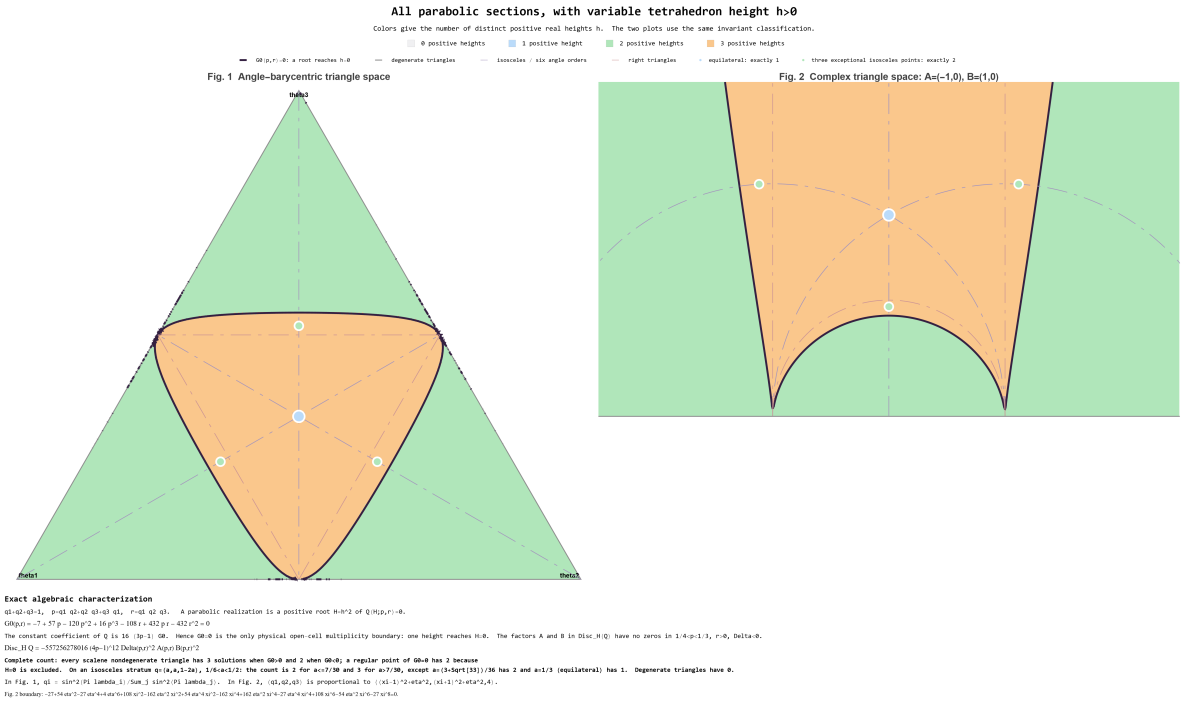

FIGURE 9. Computer-supported parabolic MPT in angle-barycentric and normalized similarity coordinates. Colors give three and two positive roots of the parabolic eliminant; global physical recovery and sign-cell connectedness are the remaining certification tasks.

9. Planar strand endpoints and the Fermat-Torricelli limit

Here "planar endpoint" means that the physical altitude z of the inverse apex above the fixed triangle plane tends to 0^+. It does *not* mean that the normalized cone-shape parameter h tends to zero. The vertex value needed later admits a direct geometric proof.

Lemma 9.1 (Vertex endpoint height)**.** *If a physical inverse-apex branch approaches vertex A, and its normalized cone parameter $H = h^2$ has a limit H_A, then necessarily $A \le 120°$ and*

$$H_A = \frac{1 + 2\cos A}{2(1 - \cos A)}. \tag{41}$$

Proof. Along every symmetric-cone realization the three unit ray vectors have common pairwise scalar product

$$\cos\beta = \frac{H - 1/2}{H + 1}$$

by Equation (1). As the apex tends to A, the unit vectors from the apex toward B and C tend respectively to $(B - A)/|B - A|$ and $(C - A)/|C - A|$. Their scalar product therefore tends to $\cos A$. Hence

$$\cos A = \frac{H_A - 1/2}{H_A + 1},$$

which solves to Equation (41). Since a physical normalized cone has $H_A \geq 0$, the formula also forces $\cos A \geq -1/2$, or $A \leq 120°$. □

The computation additionally predicts an interior planar endpoint at the Fermat–Torricelli point and the global endpoint counts below.

Computational observation 9.2 (Planar endpoint count)**.** For a nondegenerate triangle:

condition	distinct real planar limits
$\max A_i < 120°$	four: three vertices and FT
$\max A_i = 120°$	three: FT merged with that vertex
$\max A_i > 120°$	two: the other two vertices

The boundary in normalized squared sides is the union of the three equations $q_i = q_j + q_k + \sqrt{q_j q_k}$. The Fermat limiting argument, existence of every indicated vertex branch, and exhaustiveness over all real planar endpoints remain to be supplied before this observation is promoted to a theorem. The necessary vertex endpoint value itself is proved independently in Lemma 9.1.

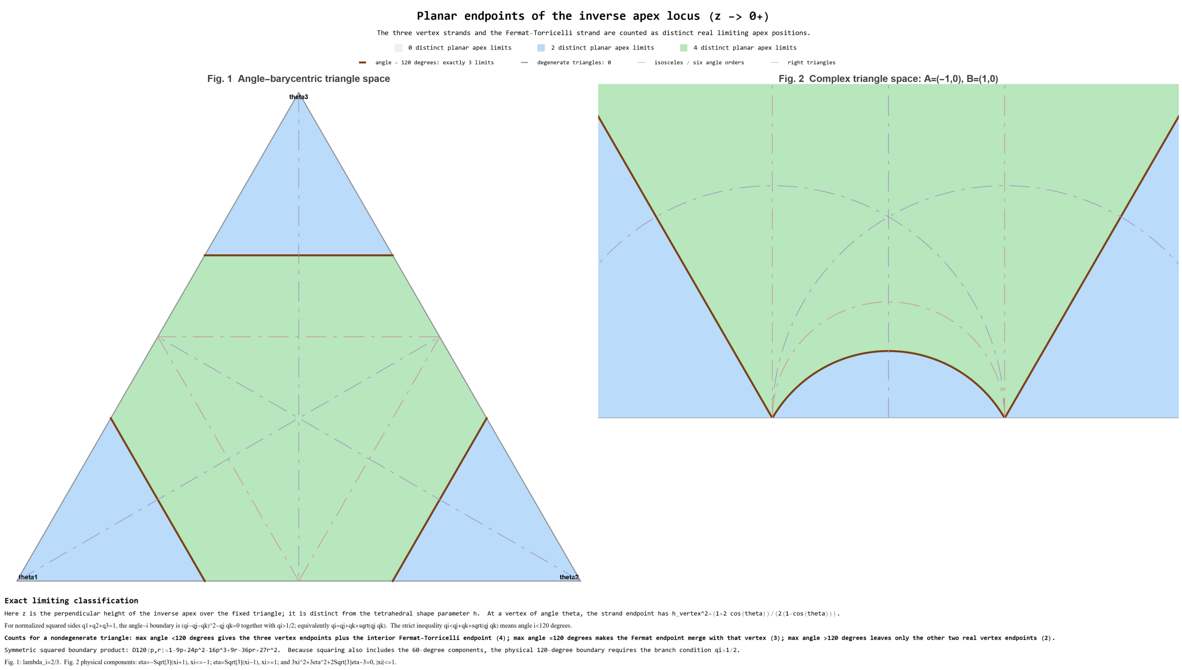

FIGURE 10. Computer-supported MPT for inverse-apex altitude $z \to 0^+$. The central region has the three vertex limits plus the Fermat-Torricelli limit. Crossing a 120° curve merges the latter with one vertex and leaves two limits.

10. TRIANGLE STRANDS AND TRIANGLE STARS

We now specialize the terminology of *The Triangle Sky* [1]. Fix a labeled triangle ABC in the plane $z = 0$ and vary h. Each connected branch of admissible apex positions is called a *triangle strand*, or a spatial *apex strand* when its ambient three-dimensional realization is being emphasized. A distinguished point on such a strand selected by an invariant simplex condition is a *triangle star*. The word *hyperstar* is reserved for analogous distinguished points associated with simplices of dimension greater than three.

Numerical continuation generically shows a branch beginning at a vertex, remaining hyperbolic until a parabolic star, and continuing elliptically through a regular star $T_5^{(j)}$; it may also meet a star $T_9^{(j)}$ at $h = \sqrt{3}$. The twelve finite critical levels are $\mathcal{H}_1, \ldots, \mathcal{H}_{12}$ according to Equation (35); actual stars and their counts use the notation $T_i^{(j)}$ and N_i fixed there. For sampled triangles with largest angle below 120°, the branch associated with that angle can bend back toward the computational Fermat–Torricelli endpoint. These are observed strand patterns, not a global existence or connectivity theorem.

Let S be the number of vertex strands, P the number of parabolic stars, and N_5 the number of regular stars $T_5^{(j)}$ at $h = \sqrt{2}$. The present exact-sampling computation on the common refinement of the three displayed MPTs gives, on every sampled open cell,

$$0 \le N_5 \le P \le S \le 3. \tag{42}$$

Consequently the observed reverse implications include $P = 3 \Rightarrow S = 3$ and $N_5 = 3 \Rightarrow P = 3$. This is not yet a proof from the pictures: a publishable proof requires the exact common cell decomposition, one certified sample per cell, and a proof that the event-curve list is complete. Until that certificate is included, Equation (42) is recorded as a computer-supported conjecture rather than a theorem. The phrase "similarly at level 2" is intentionally avoided because a bare equality count does not specify the relevant direction of implication.

The ordering of the critical levels does *not* make the fixed-height fibers nested. In particular, the tempting chain

$$S \ge P \ge N_1 \ge N_2 \ge N_3 \ge N_4 \ge N_5$$

has the following numerical counterexample candidate at its last comparison. For

$$q = \frac{1}{24001}(1173, 10317, 12511), \qquad C = \left(\frac{9144}{12511}, \frac{\sqrt{47364923}}{12511}\right),$$

high-precision physical recovery returns $N_4 = 0$ but $N_5 = 1$. Nor does the same ordering resume above the regular level: for

$$q = \frac{1}{18001}(1173, 7317, 9511), \qquad C = \left(\frac{6144}{9511}, \frac{\sqrt{33288923}}{9511}\right),$$

it returns $N_5 = 0$ but $N_6 = 1$. A weaker fan of sampled inequalities $N_i \le P$ survives for $1 \le i \le 5$, but at T_6 even that fails: the triangle

$$q = \frac{1}{18001}(6173, 6317, 5511)$$

returns $P = 3$ and $N_6 = 4$. These computations strongly indicate why the regular inequality Equation (42) is special; transition height is not a monotone coordinate on the inverse fibers. The accompanying script `certificates/TransitionStarNestingWitnesses.wl` records the rational inputs and performs high-precision physical recovery. Because that script does not isolate the roots or verify the physical inequalities in exact arithmetic, these three witnesses are numerical candidates, not certified counterexamples. The sampled fan $N_i \le P$ for $i \le 5$ is retained only as a computational conjecture.

Computational observation 10.1 (T_9-star atlas)**.** The sampled $h = \sqrt{3}$ MPT exhibits $N_9 = 0, 1, 2, 3$, and 4 physical T_9 stars. Its candidate physical boundary network consists of the three curves below. A global cell-completeness certificate has not yet been supplied, so this is not a classification theorem.

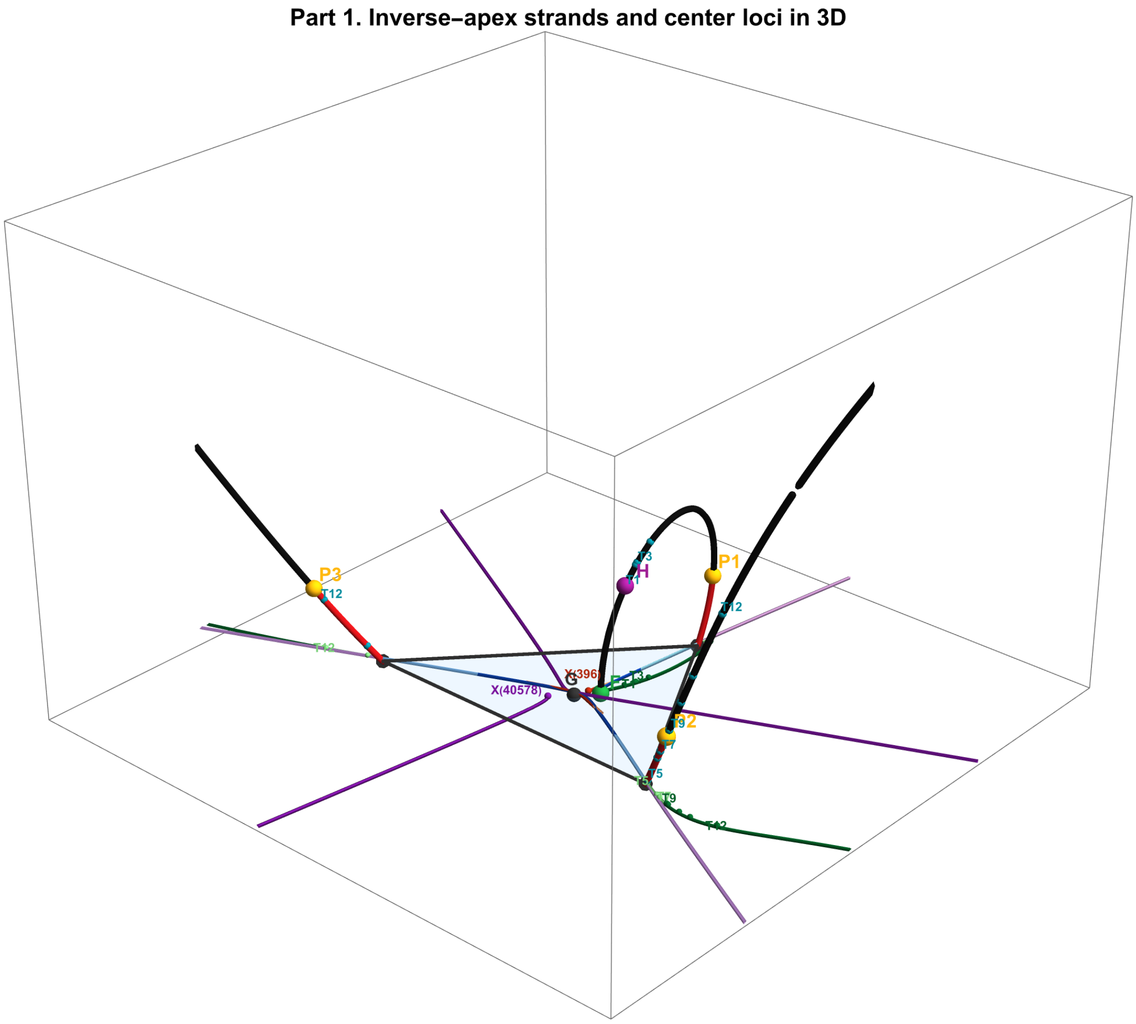

FIGURE 11. Mathematica three-dimensional inverse-apex plot for the scalene acute triangle $A = (-1, 0)$, $B = (1, 0)$, $C = (1/4, 27/20)$, exported from the default three-dimensional panel of the accompanying Mathematica application. The three spatial strands are red when hyperbolic and black when elliptic. Orange and gray curves are their orthogonal projections to the section plane. Marked points include the parabolic stars P, transition stars $T_i^{(j)}$ (with j suppressed in the graphical labels), the orthostar H, the Fermat–Torricelli endpoint F, and the centroid G. The four solid colored curves are the loci of C_1, C_2, C_3, C_4; dark and light portions correspond to elliptic and hyperbolic realizations.

In invariant coordinates the displayed boundaries are

$$\begin{aligned} F_T = & -7311616 + 65523328p - 174919056p^2 + 119246400p^3 \\ & - 57092256r + 226614024pr - 141776649r^2 = 0, \end{aligned} \tag{43}$$

$$\begin{aligned} E_T = & -4096 + 39168p - 116736p^2 + 102400p^3 - 24336r \\ & + 97344pr - 59319r^2 = 0, \end{aligned} \tag{44}$$

$$\begin{aligned} J_T = & \ 196 - 2562p + 11955p^2 - 22840p^3 + 13872p^4 + 1566r \\ & - 12420pr + 24624p^2r + 4077r^2 - 15876pr^2 = 0. \end{aligned} \tag{45}$$

Here F_T is the fold, E_T the compactified physical escape boundary, and J_T changes conic type without changing N_9 away from intersections.

Example 10.2 (Why $N_9 \not\leq N_5$)**.** For normalized squared sides

$$(q_1, q_2, q_3) = \left(\frac{1}{10}, \frac{23}{60}, \frac{31}{60}\right),$$

equivalently $C = (17/31, 2\sqrt{137}/31)$ in the complex chart, one has $N_5 = 0$ but $N_9 = 1$. This assertion has an exact certificate. At $H = 2$ the primitive candidate polynomial is

$$5819858944x^4 - 55709254144x^3 + 110526565569x^2 + 102245992496x + 23297532964,$$

and its Sturm count on $[0, 4)$ is zero. At $H = 3$ the corresponding polynomial is

$$\begin{aligned} Q_T(x) = 211309379856x^4 - 2417563180953x^3 + 1664949339019x^2 \\ + 1289627322405x + 192814376025. \end{aligned}$$

It has exactly one root x_* in $(12947/10000, 12949/10000)$ and one further real root greater than 4; its other two roots are nonreal. Put $y_* = \mu \cos 3\phi$. The common-root subresultant is the linear equation

$$\begin{aligned} 0 = {} & 8274312000x_*^5 + 288178443720x_*^4 - 3175819053562x_*^3 \\ & - 8962437318239x_*^2 + 1308057991001x_* + 1076999264932 \\ & + y_*(100707138000x_*^4 - 364022250840x_*^3 \\ & \qquad - 7131777254107x_*^2 - 4355742828449x_*). \end{aligned}$$

Thus $\mu = \sqrt{x_*}$ and $c = y_*/\sqrt{x_*}$ are exact algebraic numbers. Sturm isolation and rational interval arithmetic give $-889/1000 < c < -888/1000$ and verify all three strict inequalities Equation (4). Hence this unique T_9 realization is hyperbolic. The single branch is permitted by the compactified escape boundary $E_T = 0$, not by a two-sheet fold. Height is a shape parameter of the cone, not a nested coordinate along every apex strand; horizontal height slices therefore need not be nested.

11. Projected stars and the four distinguished-point maps

Let $\rho_A = SA$, $\rho_B = SB$, $\rho_C = SC$ and define the normalized reciprocal distance point

$$u_i = \frac{\rho_i^{-1}}{\rho_A^{-1} + \rho_B^{-1} + \rho_C^{-1}}, \qquad u_A + u_B + u_C = 1. \tag{46}$$

All barycentric coordinates in this section refer to the fixed triangle ABC. Orthogonal projection of the four spatially defined centers gives the following simple componentwise transformations.

Theorem 11.1 (Projected distinguished-point barycentrics)**.** *Up to a common homogeneous factor,*

$$C_2 = (u_A : u_B : u_C), \tag{47}$$

$$C_1 = \big(u_i(6h^2 u_i + 1 - 2h^2)\big)_{i=A,B,C}, \tag{48}$$

$$C_3 = \big(u_i(1 - 2u_i)\big)_{i=A,B,C}, \tag{49}$$

$$C_4 = \big(u_i(1 - u_i)\big)_{i=A,B,C}. \tag{50}$$

Thus $C_4 = u \odot K(u)$, where $K(u) = (1 - u_A : 1 - u_B : 1 - u_C)$ is ordinary complement and $\odot$ denotes componentwise product. Similarly $C_3 = u \odot K^{-1}(u)$ in homogeneous notation, while C_1 is the product with the homothety centered at the centroid and ratio $2h^2$.

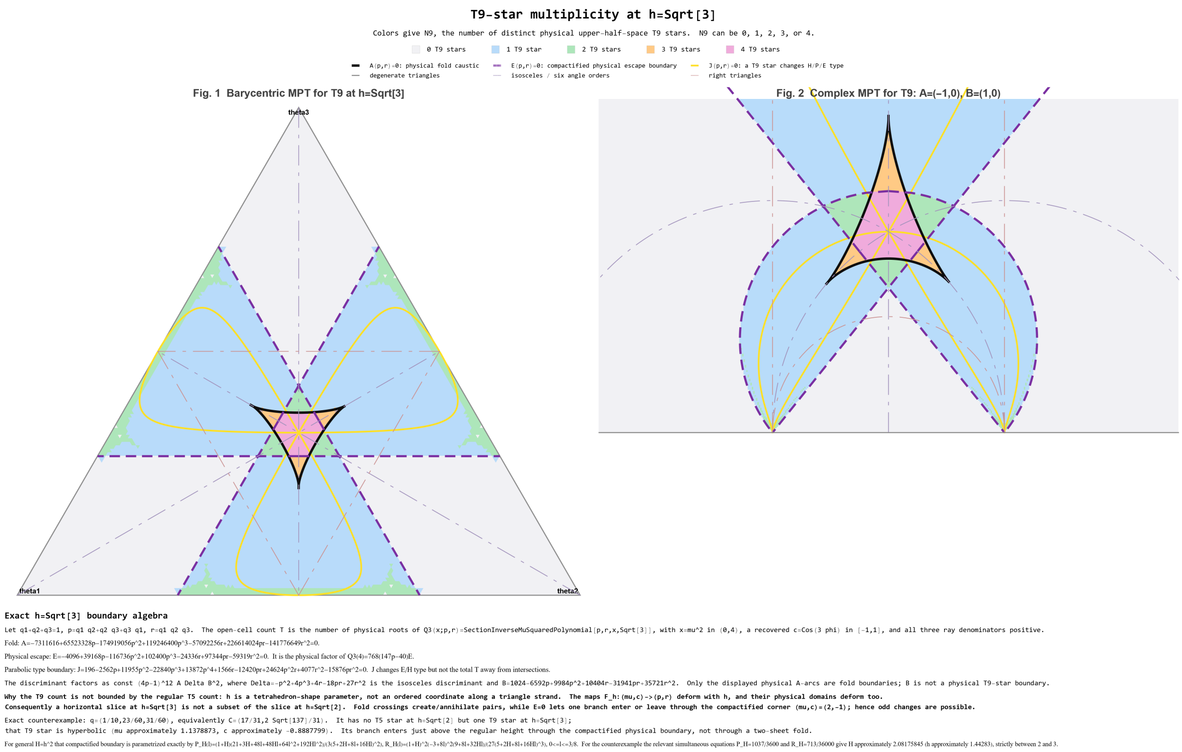

FIGURE 12. Computer-supported T_9-star MPT at $h = \sqrt{3}$. The escape curve, drawn purple and dashed, permits odd changes in the sampled count. The exact $N_5 = 0, N_9 = 1$ example is certified; global cell completeness is not yet claimed.

Proof. Put $e_i = (A_i - S)/\rho_i$. The equal-angle condition is the Gram system

$$e_i \cdot e_i = 1, \qquad e_i \cdot e_j = \gamma \quad (i \neq j).$$

Thus $n = e_A + e_B + e_C$ satisfies $n \cdot (e_i - e_j) = 0$ for every pair, so n is the symmetry-axis direction. If $\Sigma = \rho_A^{-1} + \rho_B^{-1} + \rho_C^{-1}$, its intersection with the triangle plane is

$$S + \frac{n}{\Sigma} = \frac{\rho_A^{-1} A + \rho_B^{-1} B + \rho_C^{-1} C}{\Sigma}.$$

This proves Equation (47) directly.

For the remaining points, return to the normalized forward coordinates and write $\theta_i = \phi + 2\pi i/3$. The reciprocal-distance identity used in Proposition 7.1 gives

$$3u_i = 1 - \mu \cos\theta_i, \qquad t_i = \frac{1+\mu}{3u_i}, \qquad U_2 := \sum_i u_i^2 = \frac{2+\mu^2}{6}.$$

Consider homogeneous barycentrics $\lambda_i = u_i(a + bu_i)$. The identities

$$\sum_i \cos\theta_i = \sum_i \sin\theta_i = \sum_i \sin\theta_i \cos\theta_i = 0, \qquad \sum_i \cos^2\theta_i = \frac{3}{2}$$

show that their affine point lies on the distinguished u-axis. Since $\sum_i \lambda_i = a + bU_2$, its signed intrinsic coordinate is

$$q(a,b) = d\left(1 - \frac{\mu(1+\mu)b}{6(a+bU_2)}\right). \tag{51}$$

The four choices

point	(a,b)	$q(a,b)$
C_2	$(1,0)$	d
C_1	$(1-2h^2, 6h^2)$	$(1-h^2\mu)/d$
C_3	$(1,-2)$	$d/(1-\mu)$
C_4	$(1,-1)$	$d(4+\mu)/(4-\mu^2)$

reproduce exactly the four coordinates in Equation (9). Their barycentric weights $u_i(a+bu_i)$ are therefore respectively Equations (47) to (50). ☐

In the broad, transformation-theoretic meaning used in triangle geometry, the orthogonal projection of a triangle star is therefore essentially a triangle center: it is constructed from ABC alone and is equivariant under similarities and relabelings. When a star level has three branches, its three projections form a central triangle rather than a single-valued center.

The orthostar H is the star $T_1^{(j)}$ at $h = 1/\sqrt{2}$, and Equation (48) reduces to the orthocenter. Thus the orthogonal projection of H is exactly the orthocenter, explaining the label used in the figures. The parabolic and transition-star projections $T_i^{(j)}$ are obtained from the same formula at their respective levels $\mathcal{H}_i$; every three-valued system is a central triangle, equivariant under every relabeling of ABC. Our exact search did not find the parabolic, T_5, and T_9 central triangles as named entries in the ETC data examined. Because the ETC evolves, the appropriate claim is "no match found", not "absent for all time" [8, 9].

The endpoint formula also removes apparent numerical gaps in the C_3 and C_4 loci. If a strand tends to A, put $b = CA$ and $c = AB$. From $u_A = 1-\varepsilon(1/b+1/c)+o(\varepsilon)$, $u_B = \varepsilon/c+o(\varepsilon)$, and $u_C = \varepsilon/b + o(\varepsilon)$, Equation (50) gives

$$C_4 \longrightarrow \left(\frac{1}{2} : \frac{b}{2(b+c)} : \frac{c}{2(b+c)}\right). \tag{52}$$

This is the midpoint of A and the foot of the internal A-angle bisector; the other two vertex limits follow cyclically.

At an interior Fermat–Torricelli endpoint let $f = (f_A : f_B : f_C)$ be the normalized barycentrics of $F = X(13)$, so that $f_i \propto 1/FA_i$ and $\sum_i f_i = 1$. Equations (47), (49) and (50) then give the three distinct finite limits

$$C_2 \longrightarrow X(13), \qquad C_3 \longrightarrow (f_i(1-2f_i)) = X(40578), \qquad C_4 \longrightarrow (f_i(1-f_i)) = X(396). \tag{53}$$

The ETC descriptions are, respectively, the first Fermat point, the $X(2)$-Ceva conjugate of $X(13)$, and $X(396)$ [9]. For the default triangle, the C_3 limit has Cartesian coordinates $(0.01209042, 0.30703738)$, agreeing with the independently continued strand. At the opposite prism limit $u_i \to 1/3$, so C_2, C_3, C_4 all converge to the centroid G; only the two prism-ending branches are completed there.

Proposition 11.2 (C_3 poles and C_4 finiteness)**.** *Along every analytic star branch,*

$$\sum_i u_i(1-2u_i) = \frac{1-\mu^2}{3}, \qquad \sum_i u_i(1-u_i) = \frac{4-\mu^2}{6}. \tag{54}$$

Consequently C_3 has a simple projective pole at each generic parabolic star $\mu = 1$, whereas C_4 remains finite throughout $0 \le \mu < 2$. The two affine arms of C_3 adjacent to a parabolic star tend to opposite rays of one asymptotic line. Its direction is the line through the finite parabolic points C_2 and C_4.

Proof. The identity $\sum_i u_i^2 = (2+\mu^2)/6$ gives Equation (54) immediately. At $\mu = 1$ the unnormalized C_3 vector has barycentric sum zero and therefore represents a point at infinity. In Cartesian notation its direction is $d = \sum_i u_i(1-2u_i)A_i$. Since at the same parabolic star

$$C_2 = \sum_i u_i A_i, \qquad C_4 = 2\sum_i u_i(1-u_i)A_i,$$

one has $C_2 - C_4 = -d$. Analytic continuation through the simple zero of the first denominator changes its sign, giving the two opposite rays. The second denominator is positive for $0 \le \mu < 2$. □

For the three parabolic branches, let $d_j = C_{2,j} - C_{4,j}$ and put $\alpha_j = \arg(d_{j,x} + i d_{j,y}) \pmod{\pi}$. Sorting the three α_j and taking successive differences, including the wrap by π, gives the three angles between the unoriented asymptotic lines. For the default triangle the line orientations are

$$22.9921^\circ, \qquad 81.2326^\circ, \qquad 151.9333^\circ,$$

and the cyclic sectors are

$$58.2406^\circ, \qquad 70.7007^\circ, \qquad 51.0588^\circ.$$

Thus the three asymptotic lines are not generally separated by 60°.

12. The quintic shadow of the apex strands

Eliminating the apex height and common ray angle from the equal-angle conditions gives a surprisingly small equation for the C_2 shadow.

Theorem 12.1 (Axis-intersection quintic containment)**.** *Let $(x : y : z)$ be barycentrics in ABC, with $a = BC$, $b = CA$, $c = AB$. The projected physical C_2 locus is contained in*

$$\begin{aligned} 0 = {} & a^2 yz(z-y)(x^2 - yz) + b^2 zx(x-z)(y^2 - zx) \\ & + c^2 xy(y-x)(z^2 - xy). \end{aligned} \tag{55}$$

At points with $xyz \neq 0$ where the first two coefficient columns of the cosine-law system have rank two, vanishing of this quintic is also sufficient for a complex solution (τ^{-2}, γ). No converse is asserted at the rank-one locus or on the coordinate lines, and generic irreducibility and the precise Zariski closure are left open.

Proof. Let γ be the common cosine of the three edge angles at the apex and write $\rho_A = \tau/x$, $\rho_B = \tau/y$, $\rho_C = \tau/z$, as permitted by Equation (47). The three cosine-law equations become

$$\begin{aligned} a^2 y^2 z^2 \tau^{-2} + 2yz\gamma &= y^2 + z^2, \\ b^2 z^2 x^2 \tau^{-2} + 2zx\gamma &= z^2 + x^2, \\ c^2 x^2 y^2 \tau^{-2} + 2xy\gamma &= x^2 + y^2. \end{aligned}$$

They are linear in the two unknowns τ^{-2} and γ. Hence the determinant of the three columns

$$\begin{pmatrix} a^2y^2z^2 & 2yz & -(y^2+z^2) \\ b^2z^2x^2 & 2zx & -(z^2+x^2) \\ c^2x^2y^2 & 2xy & -(x^2+y^2) \end{pmatrix}$$

vanishes. Expanding it and removing the coordinate-line factor $2xyz$ gives exactly Equation (55), proving containment.

If the first two columns have rank two, determinant zero is equivalent to the augmented matrix having rank at most two; hence the two unknowns τ^{-2} and γ exist and are obtained from any nonsingular 2×2 row minor. This argument fails on the rank-one locus. In particular, at $(x : y : z) = (a^2 : b^2 : c^2)$ those two columns are proportional, and determinant zero alone does not imply consistency with the third column. Coordinate-line points require separate homogenized analysis as well. The rank-two converse in the statement is therefore the strongest conclusion justified by this determinant calculation; saturation of the rank-one and coordinate-line ideals is a remaining task. □

The visible "complement" phenomenon is now precise. The C_1 shadow and the C_2 quintic arcs continue through a vertex with the same tangent, so together they form a visually smooth graph. They are not, however, one analytic curve in a generic scalene triangle.

Theorem 12.2 (Curvature jump at a vertex)**.** *At vertex A, put $u = \cos A$, $m = \cos(A/2)$, $n = \sin(A/2)$ and assume the generic scalene acute case $b \neq c$, $u \neq 0$. Choose local Cartesian coordinates centered at A, with the X-axis the internal angle bisector. Orient the common X-axis positively and define κ_i to be the signed* graph *curvature of $Y_i(X)$ at the origin. For a parameter $s \to 0^+$ the two branches have*

$$\kappa_2 = \frac{(b-c)un}{2bcm^2}, \qquad \kappa_1 = -\frac{(b-c)n(1+u)^3}{2bcm^2u^2}, \tag{56}$$

and therefore

$$\boxed{\frac{\kappa_1}{\kappa_2} = -\left(\frac{1+\cos A}{\cos A}\right)^3.} \tag{57}$$

The union is C^1 but not C^2, and hence not analytic, at A.

Proof. With barycentric coordinates λ_i for C_2, solve the equal-angle cosine-law system displayed in the proof of Theorem 12.1 to second order:

$$\lambda_B = s,$$
$$\lambda_C = \frac{c}{b}s + \frac{(b-c)c\cos A}{b^2}s^2 + O(s^3).$$

Conversion to the bisector frame gives

$$X_2 = 2cm\,s + \frac{(b-c)cum}{b}s^2 + O(s^3),$$
$$Y_2 = \frac{(b-c)cun}{b}s^2 + O(s^3).$$

By Lemma 9.1, the endpoint height is $H_A = (1+2u)/(2(1-u))$. Substitution in Equation (48) gives

$$X_1 = -\frac{2cmu}{1+u}s + O(s^2),$$
$$Y_1 = -\frac{(b-c)cn(1+u)}{b}s^2 + O(s^3).$$

For $X = a_1 s + O(s^2)$ and $Y = b_2 s^2 + O(s^3)$, the signed graph curvature with respect to the common positive X-direction is $2b_2/a_1^2$. This convention is independent of whether the branch parameter s makes X increase or decrease, and yields Equations (56) and (57). ☐

If $b = c$, both curvatures vanish and both branches lie on the symmetry bisector. At $A = 90°$ the C_1 linear term vanishes, so the generic comparison is singular. The same formal expansion for $90° < A < 120°$ predicts same-side tangency. In the computational endpoint picture of Section 9, the Fermat branch merges with the vertex at $120°$; neither statement is used in the acute-case theorem above.

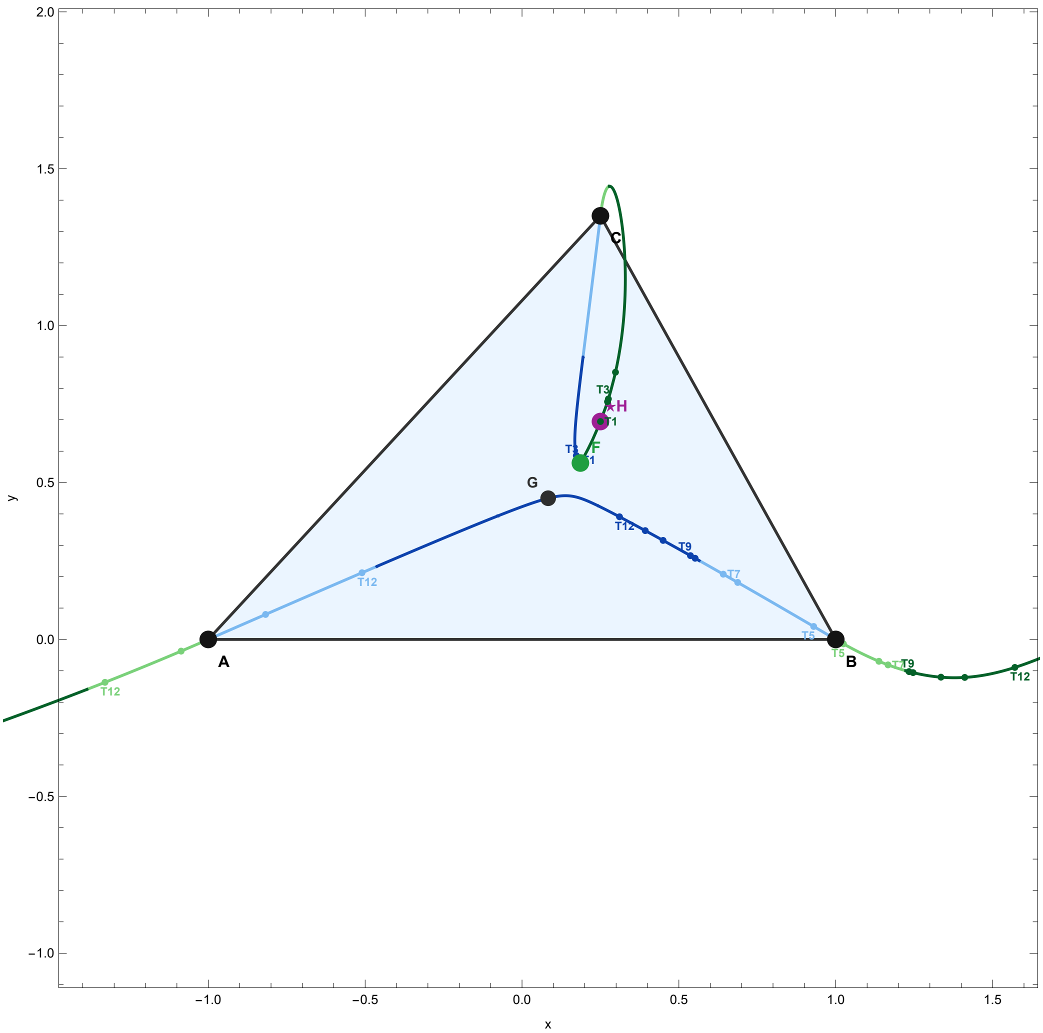

FIGURE 13. Default triangle-plane panel of the strand application for $A = (-1, 0)$, $B = (1, 0)$, and $C = (1/4, 27/20)$, restricted to the C_1 and C_2 loci. Small points mark their transition-center images; only $T_1, T_3, T_5, T_7, T_9, T_{12}$ are labeled. The branches meet at the vertices with a common tangent, while Equation (57) proves that their signed curvatures jump. The two prism branches of C_2 meet at G, whereas its numerically continued largest-angle branch ends at $F = X(13)$.

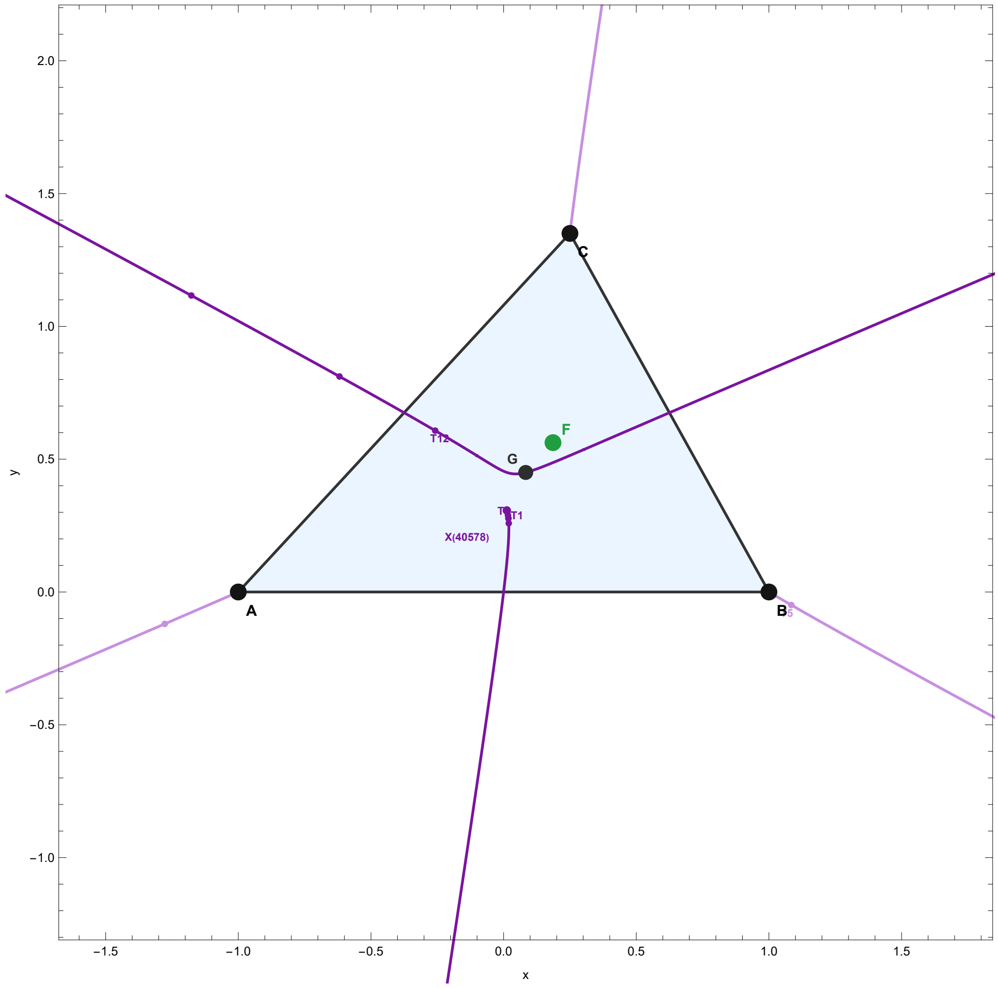

FIGURE 14. The same triangle restricted to the C_3 locus. Each parabolic star produces one projective pole, with its elliptic and hyperbolic arms approaching opposite ends of the asymptotic line described in Proposition 11.2. The two prism branches meet at G; the numerically continued largest-angle branch instead has the finite planar endpoint $X(40578)$ from Equation (53).

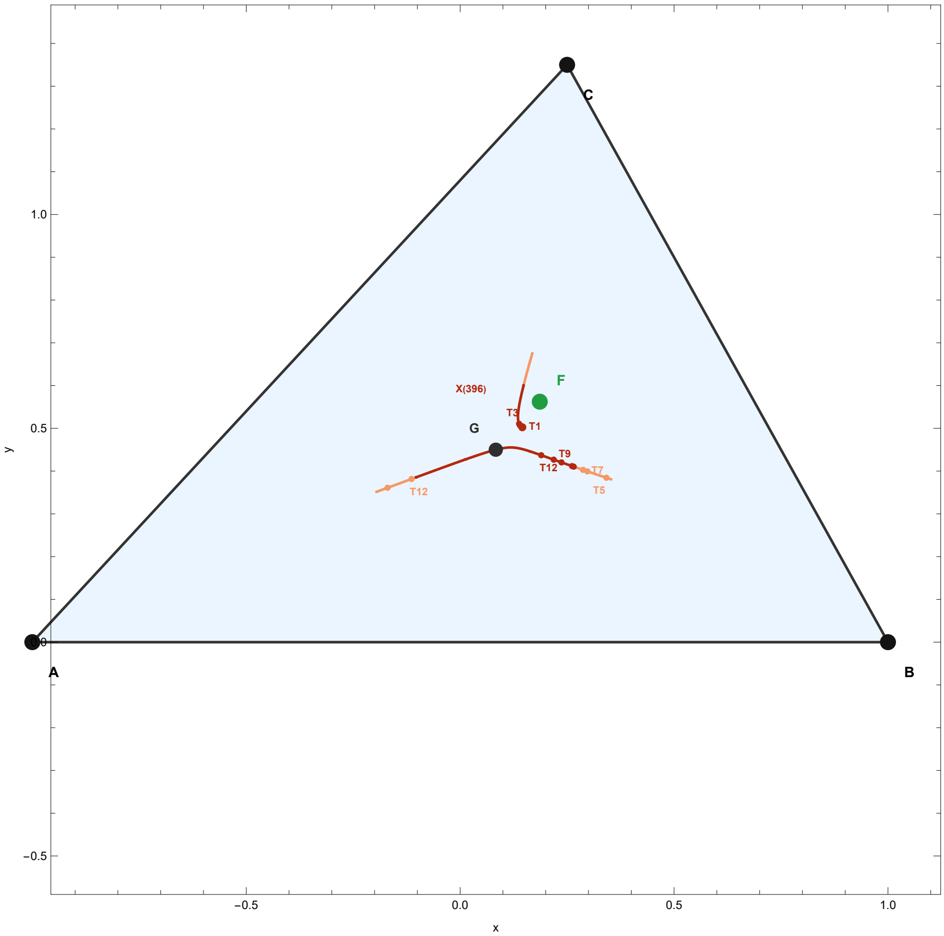

Figure 15. The same triangle restricted to the bounded C_4 locus. Its vertex limits are the angle-bisector midpoints in Equation (52); its two prism branches meet at G; and its numerically continued largest-angle branch ends at $X(396)$ as in Equation (53). The absence of a parabolic pole follows from the second denominator in Equation (54).

13. How to read and color an MPT

An MPT is not obtained reliably by coloring a rectangular pixel grid and then guessing boundaries. The robust procedure is real-algebraic, following the standard discriminant-variety and cell-decomposition viewpoint [11].

(1) Compute every algebraic event curve: discriminant/fold, parabolic type, escape, degenerate boundary, isosceles seams, and special endpoint factors.
(2) Compute their intersections and self-intersections, and form the connected cells of the complement inside legitimate triangle space.
(3) Choose one certified sample point per cell. Isolate the real roots of the inverse polynomial exactly, recover c, and apply all positivity filters.
(4) Propagate that label to the whole cell. Root counts cannot change away from the event curves. High-resolution raster coloring is then only a rendering device, not the mathematical classifier.

This explains both why coloring is possible and why a first attempt can be slow. Once the algebraic cell decomposition and sample labels are cached, interactive displays should begin with the quick boundary-only version and enable filled regions as an option. Orbits are overlays: thin light curves, with the ϕ-orbit and the fixed-ϕ α-orbit both passing through the displayed triangle. The six angle-order seams are light dashed lines; right-angle and isosceles loci are light dash-dotted guides. They are not inverse multiplicity boundaries unless an algebraic event curve coincides with them.

14. Synthesis and open directions

The spatial section problem is governed by three interacting geometries. First, the forward map Equations (3) and (5) is elementary and its conic type is the single comparison $\mu \lesseqgtr 1$. Second, the inverse map is a real-algebraic fiber problem: a quartic supplies candidates, while discriminant, escape, and positivity conditions decide what is physically present. Third, numerical continuation organizes inverse fibers into strands whose shadows and four distinguished-point maps belong naturally to triangle geometry.

The regular tetrahedron is therefore one distinguished horizontal slice, not the whole phenomenon. The computed h-families expose two mechanisms invisible in that slice: a branch may be created in a fold pair, or may enter singly through the compactified physical edge. The certified example $N_5 = 0, N_9 = 1$ proves non-nesting without asserting completeness of the T_9-star MPT. Pinchon's additional values $a_{\mathrm{P}} = a_0$ and $a_{\mathrm{P}} = \sqrt{2}$ are now identified as two fold–escape changes of total multiplicity. Exact analysis of the parabolic divider adds six previously missed incidences and proves the complete symmetry-marked twelve-height refined theorem Theorem 7.8. The phase atlas Figures 5 to 8 samples all thirteen open phases. The computer-supported planar-altitude limit predicts the Fermat–Torricelli endpoint and the 120° boundary, while the rigorous prism limit identifies the conic pair with the Steiner ellipses and collapses three distinguished points to the centroid.

Several directions remain attractive. The central triangles formed by the parabolic and transition-star projections deserve comparison with future ETC releases and with known triangle cubics. A synthetic derivation of the C_2 quintic and of the curvature ratio would complement the elimination proofs. The explicit order-three Poncelet map of Theorem 3.2 also suggests studying the full conic pencil and its degeneration at the affine parabolic chart, independently of the forward-ray truncation. The remaining global questions concern the parabolic-height, planar-endpoint, and fixed-transition-star atlases rather than the now-complete symmetry-marked fixed-height refined event network.

Acknowledgements and AI assistance

The author thanks Mowaffaq Hajja for his continuous support and inspiring discussions. In 2024, he introduced the author to this problem and shared with him recollections of his correspondence with Folke Eriksson in the 1990s. The author first became aware of Pinchon's and Xia–Yang's work in August 2026 and revised the historical and precedence claims accordingly. The terms *triangle star*, *triangle strand*, and *triangle hyperstar* were developed in the unpublished project *The Triangle Sky*, current version 3.14 (2026) [1]. The research and revision process was assisted by generative-AI systems, principally ChatGPT and, to a lesser extent, Gemini, for bibliographic search, symbolic-computation support, code development, and editorial suggestions. These systems are tools, not coauthors: the author independently reviewed the mathematics, selected and verified every claim included in the manuscript, and accepts full responsibility for the paper's contents, errors, and attributions.

Reproducibility note

All displayed algebraic boundaries were produced from exact rational functions and polynomials before numerical rendering. Region colors whose global cell proof is incomplete are labeled computational observations rather than classifications. The accompanying Wolfram Language package implements the forward vertices and angles, physical filters, conics, centers, invariant maps, regular exact inverse conditions, general fixed-height inverse quartic, parabolic height quintic, planar endpoints, and the MPT atlas generators. Numerical values in the text are explanatory only; none is used to define a boundary or to certify a count.

The certificate files in `certificates/` target Wolfram Language 15.0. In particular, the refined-transition certificate checks the embedded parabolic, fold, and escape parametrizations, endpoint and discriminant factorizations, triple-incidence resultants, Sturm counts, and exact ordering used in Theorem 7.8. The file `PonceletReturnMap.wl` independently checks the two conic substitutions, agreement with the spatial vertex parametrization, chord tangency, the Möbius cube, and the double-line pencil identity. The accompanying `SUPPLEMENT-README.md` records exact run commands, expected output, approximate runtimes, and SHA-256 hashes. A result whose complete event-curve, physical-recovery, or cell-decomposition certificate has not yet been included is explicitly labeled a computational observation or conjecture. The source, certificates, figure generators, and compiled manuscript are deposited together as the public versioned release `ismaa3iil/tetrahedral-sections`, v1.0.0. Its SHA-256 manifest identifies the exact files accompanying the journal submission.

References

[1] I. Hammoudeh, *The Triangle Sky*, version 3.14, unpublished manuscript, 2026.

[2] J.-V. Poncelet, *Traité des propriétés projectives des figures*, Bachelier, Paris, 1822.

[3] V. Dragović and M. Radnović, *Poncelet Porisms and Beyond: Integrable Billiards, Hyperelliptic Jacobians and Pencils of Quadrics*, Frontiers in Mathematics, Birkhäuser/Springer, Basel, 2011. doi:10.1007/978-3-0348-0015-0.

[4] D. Kalman, *An elementary proof of Marden's theorem*, Amer. Math. Monthly **115** (2008), no. 4, 330–338. doi:10.1080/00029890.2008.11920532.

[5] F. Eriksson, *Which triangles are plane sections of regular tetrahedra?*, Amer. Math. Monthly **101** (1994), no. 8, 788–789. doi:10.1080/00029890.1994.11997028.

[6] D. Pinchon, *Les sections planes d'un triedre regulier*, manuscript, December 1991; Prepublication 92-12, Institut de Mathematiques de Rennes, June 1992, 53 pp.

[7] B. Xia and L. Yang, *An algorithm for isolating the real solutions of semi-algebraic systems*, J. Symbolic Comput. **34** (2002), 461–477. doi:10.1006/jsco.2002.0572.

[8] C. Kimberling, *Triangle Centers and Central Triangles*, Congressus Numerantium **129**, Utilitas Mathematica, 1998.

[9] C. Kimberling, *Encyclopedia of Triangle Centers*, online database, `https://faculty.evansville.edu/ck6/encyclopedia/ETC.html`, accessed August 2026.

[10] M. Berger, *Geometry I*, Springer, Berlin, 1987.

[11] S. Basu, R. Pollack, and M.-F. Roy, *Algorithms in Real Algebraic Geometry*, 2nd ed., Springer, 2006.

[12] M. Coste and M. Shiota, *Thom's first isotopy lemma: a semialgebraic version, with uniform bound*, in *Real Analytic and Algebraic Geometry*, de Gruyter, Berlin, 1995, 83–102. doi:10.1515/9783110881271.83.